Conceptual Design of the Lunar Crater Radio Telescope (LCRT) on the Far Side of the Moon

Saptarshi Bandyopadhyay
Jet Propulsion Laboratory
California Institute of Technology
4800 Oak Grove Dr,
Pasadena, CA 91109
+1-626-318-4174
Saptarshi.Bandyopadhyay@jpl.nasa.gov

Patrick Mcgarey
Jet Propulsion Laboratory
California Institute of Technology
4800 Oak Grove Dr,
Pasadena, CA 91109
+1-626-658-0505
Patrick.Mcgarey@jpl.nasa.gov

Ashish Goel
Jet Propulsion Laboratory
California Institute of Technology
4800 Oak Grove Dr,
Pasadena, CA 91109
+1-626-660-4714
Ashish.Goel@jpl.nasa.gov

Ramin Rafizadeh
Jet Propulsion Laboratory
California Institute of Technology
4800 Oak Grove Dr,
Pasadena, CA 91109
+1-626-517-3970
Ramin.Rafizadeh@jpl.nasa.gov

Melanie Delapierre
Jet Propulsion Laboratory
California Institute of Technology
4800 Oak Grove Dr,
Pasadena, CA 91109
Melanie.Delapierre@jpl.nasa.gov

Manan Arya
Jet Propulsion Laboratory
California Institute of Technology
4800 Oak Grove Dr,
Pasadena, CA 91109
Manan.Arya@jpl.nasa.gov

Joseph Lazio
Jet Propulsion Laboratory
California Institute of Technology
4800 Oak Grove Dr,
Pasadena, CA 91109
+1-818-354-4198
Joseph.Lazio@jpl.nasa.gov

Paul Goldsmith
Jet Propulsion Laboratory
California Institute of Technology
4800 Oak Grove Dr,
Pasadena, CA 91109
+1-818-393-0518
Paul.F.Goldsmith@jpl.nasa.gov

Nacer Chahat
Jet Propulsion Laboratory
California Institute of Technology
4800 Oak Grove Dr,
Pasadena, CA 91109
+1-818-354-3908
Nacer.E.Chahat@jpl.nasa.gov

Adrian Stoica
Jet Propulsion Laboratory
California Institute of Technology
4800 Oak Grove Dr,
Pasadena, CA 91109
+1-818-354-2190
Adrian.Stoica@jpl.nasa.gov

Marco Quadrelli
Jet Propulsion Laboratory
California Institute of Technology
4800 Oak Grove Dr,
Pasadena, CA 91109
+1-818-354-7548
Marco.B.Quadrelli@jpl.nasa.gov

Issa Nesnas
Jet Propulsion Laboratory
California Institute of Technology
4800 Oak Grove Dr,
Pasadena, CA 91109
+1-818-354-9709
Issa.A.Nesnas@jpl.nasa.gov

Mr. Kenneth Jenks
NASA Lyndon B. Johnson Space Center
Houston, Texas, 77058, USA
kenneth.c.jenks@nasa.gov

Gregg Hallinan
Division of Physics, Mathematics and Astronomy
California Institute of Technology
1200 E California Blvd,
Pasadena, CA 91125
gh@astro.caltech.edu

Abstract—An ultra-long-wavelength radio telescope on the far side of the Moon has significant advantages compared to Earth-based and Earth-orbiting telescopes, including:

1. Enabling observations of the Universe at wavelengths longer than 10 meters (i.e., frequencies below 30 MHz), wavelengths at which critical cosmological or extrasolar planetary signatures are predicted to appear, yet cannot be observed from the ground due to absorption from the Earth's ionosphere; and
2. The Moon acts as a physical shield that isolates a far-side lunar-surface telescope from radio interference from sources on the Earth's surface, the ionosphere, Earth-orbiting satellites, and the Sun's radio emission during the lunar night.

In this paper, we present the conceptual design of the Lunar Crater Radio Telescope (LCRT) on the far side of the Moon. We propose to deploy a wire mesh using wall-climbing DuAxel robots in a 3–5 km diameter crater, with a suitable depth-to-diameter ratio, to form a parabolic reflector with a 1 km diameter. LCRT will be the largest filled-aperture radio telescope in the Solar System; larger than the former Arecibo telescope (305 m diameter, 3 cm - 1 m wavelength band, 0.3–10 GHz frequency band) and the Five-hundred-meter Aperture Spherical radio Telescope (FAST) (500 m diameter, 0.1-4.3 m wavelength band, 60-3000 MHz frequency band). LCRT's science objective is to track the evolution of the neutral intergalactic medium before and during the formation of the first stars in the 10–100 m wavelength band (3–30 MHz frequency band), which is consistent with priorities identified in the Astrophysics decadal survey. We describe LCRT's science objectives and the key technology challenges that need to be overcome to make this concept a reality. We envisage that LCRT will open a new window for humanity's exploration of the Universe.

TABLE OF CONTENTS

1. INTRODUCTION

An ultra-long-wavelength radio telescope on the far-side of the Moon has significant advantages compared to Earth-based and Earth-orbiting telescopes, including:

• Enabling observations of the Universe at wavelengths longer than 10 meters (i.e., frequencies below 30 MHz), wavelengths at which critical cosmological signatures from the "Dark Ages" are predicted to appear, yet cannot be observed from the ground due to absorption from the Earth's ionosphere; and
• The Moon acts as a physical shield that isolates a lunar-surface telescope from radio interference from sources on the Earth's surface, the ionosphere, Earth-orbiting satellites, and the Sun's radio emission during the lunar night.
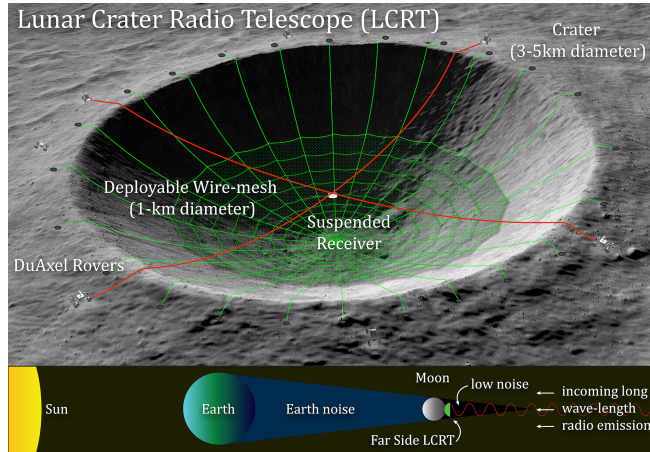

Figure 1: Notional view of LCRT on the far-side of the Moon
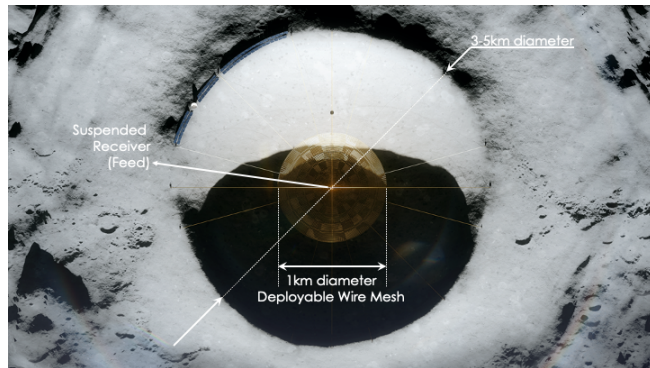

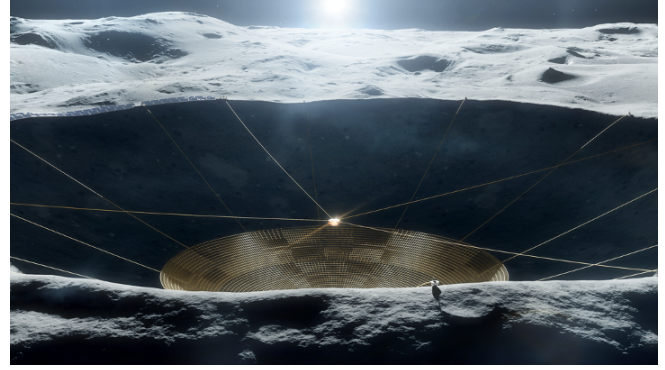Figure 2: Concept art of LCRT - Top View (artist Vladimir Vustyansky)

Figure 3: Concept art of LCRT - Side View (artist Vladimir Vustyansky)

In this paper, we present the conceptual design of a Lunar Crater Radio Telescope (LCRT) on the far side of the Moon. We propose to deploy a wire mesh using wall-climbing Du-Axel robots in a 3–5 km diameter lunar crater on the far side, with suitable depth-to-diameter ratio, to form a parabolic reflector with a 1 km diameter (Fig. 1,2,3). LCRT will be the largest filled-aperture radio telescope in the Solar System; larger than the Arecibo telescope (305 m diameter, 3 cm–1 m wavelength band, 0.3 GHz–10 GHz frequency band) [1] and the Five-hundred-meter Aperture Spherical radio Telescope (FAST) (500 m diameter, 0.1–4.3 m wavelength band, 60 MHz–3000 MHz frequency band) [2] on Earth. LCRT could enable scientific discoveries in the field of cosmology by observing the early Universe in the 10–50 m wavelength band (i.e., 6–30 MHz frequency band), which has not been explored for cosmological observations to date.

Literature Survey

Arecibo-type *lunar-crater-telescope concept* studies in the 1990s had proposed suspending cables over existing lunar craters (Fig. 4) [3], [4]. These studies flagged significant technical challenges (Table 1) and concluded that the lunar-crater-telescope concept was not feasible. In this paper, we address these challenges using novel technologies (Table 1) and show that the LCRT concept is now feasible.
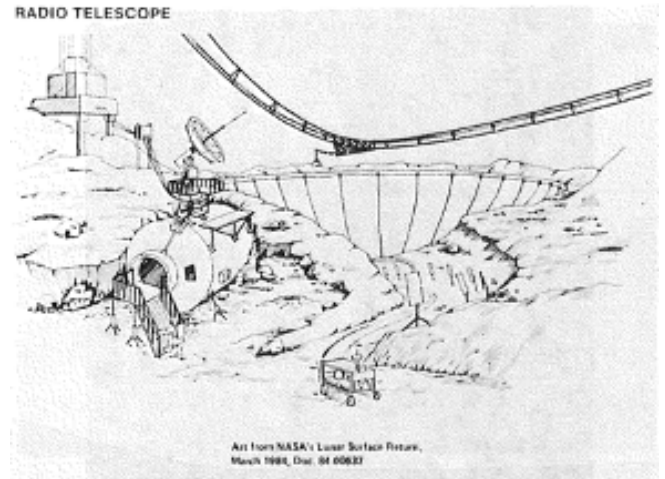

Figure 4: Arecibo-type lunar-crater-telescope concept from 1990s

Sparse dipole array concepts such as FARSIDE (Farside

Technical challenges for a lunar crater telescope concept [4]	Our innovations that enable LCRT
(i) Selection of existing lunar crater is difficult	Identified craters of suitable depth, with appropriate depth-to-diameter ratio, using high-resolution lunar maps.
(ii) Arecibo-type foundation elements, support structures, and tension/shear resistant anchors for cables are too heavy, (iii) Design of thermal strain compensation system is difficult	Leveraging the Moon's low gravity, we designed a reflective dish using variable-thickness wire-mesh (mass 1200 kg), which passively maintains the desired shape across large thermal fluctuations ($100°$C to $-173°$C) over a lunar day, and that is suspended inside the crater; the LCRT has no moving parts and needs no foundation elements or support structures, making it mass-effective and cost-effective.
(iv) Rim to floor transportation is difficult	Employ high-TRL DuAxel robots, capable of climbing/descending cliff faces on the Moon.

Table 1: Key Innovations of the LCRT concept

Array for Radio Science Investigations of the Dark ages and Exoplanets) [5], VLFA (Very Low Frequency Array) [6], ROLSS (Radio Observatory for Lunar Sortie Science) [7], and DALI (Dark Ages Lunar Interferometer) [8]; *lunar-orbiting satellite mission concepts* like LORAE (Lunar Observer Radio Astronomy Experiment) [9], DARE (Dark Ages Radio Explorer) [10]; and *multi-satellite mission concepts in the Earth-Moon L2 Lagrange point* like ALFA (Astronomical Low-Frequency Array) [11], FIRST (Formation-flying sub-Ionospheric Radio astronomy Science and Technology)[12], OLFAR (Orbiting Low Frequency Antennas for Radio Astronomy) [13] have smaller collecting areas than a lunar-crater telescope. In this paper, we present a cost- and mass-effective strategy for building the Lunar Crater Radio Telescope (LCRT) concept.

2. SCIENCE OBJECTIVES OF LCRT

LCRT's science objective is to track the evolution of the neutral intergalactic medium (IGM) before and during the formation of the first stars, which is consistent with priorities identified in the decadal survey [14], [15]. These observations are difficult, if not impossible, to conduct from Earth due to ionospheric absorption and reflection [16], [17].

Dark Ages and Cosmic Dawn—The 2010 Decadal Survey [14] identified "Cosmic Dawn" as one of three key science objectives, and a Cosmic Dawn Mapper aimed at exploring these epochs was identified in the Astrophysics roadmap [15]. Following recombination (redshift $z \approx 1100$), the Universe entered a largely neutral state in which neutral hydrogen (HI) was the dominant baryonic component of the intergalactic medium (IGM). The highly redshifted hyperfine transition of HI ($\lambda = 21$ cm, $\nu = 1420$ MHz) provides unique information about the state of the IGM and large-scale structures during the formation of the first stars and potentially can probe the IGM prior to their formation. Multiple epochs can be identified [19], [20] associated with the true "Dark Ages," the epoch of the formation of the first stars, the epoch of first heating (likely from accreting black holes), and the Epoch of Reionization. A crucial feature of this HI signal is that it allows the evolution of the Universe to be tracked by studying the signal at different redshifts. In contrast, the cosmic microwave background is a continuum measurement at essentially a single redshift, providing a single snapshot view of the Universe [21]. There are emerging constraints on the evolution of the IGM during First Heating and the Epoch of Reionization [22], [23], [24], but the Dark Ages ($z \approx 70$; $\nu \approx 20$ MHz) and the First Stars ($z \approx 40$; $\nu \approx 35$ MHz) epochs remain both exciting and unlikely to be constrained significantly from the ground.

During the Dark Ages, the Universe was considerably simpler, consisting mainly of neutral hydrogen, photons, and dark matter. It therefore serves as an excellent laboratory for testing our fundamental understanding of cosmology, dark matter physics and inflation. Due to cosmological redshift, this 21cm signal from the Dark Ages is currently visible at ultra-long radio wavelengths of 10m or more. Fig. 6 shows our best understanding of the 21cm line, as a function of cosmological redshift or frequency [25]. Going towards the left in this plot is equivalent to going further back in time. The signals from the Dark Ages (< 20 MHz) and First Stars (60–100 MHz) arrive at different frequencies. The dotted line is based on a theoretical cosmological model of the early Universe, without any astronomical sources like stars or galaxies. Recent measurements using the EDGES instrument in Australia have constrained the signals from the first stars [24], [26]. This region is highlighted in gray. Different phenomenological models (shown in different colors) have been proposed to match the EDGES signal which leads to large variations in their prediction of the absorption trough corresponding to the signal from the Dark Ages. LCRT will collect data about Dark Ages to constrain these models. LCRT's data will help constrain or bound our understanding of fundamental aspects of the Universe, like: (i) State of the intergalactic medium, (ii) Large-scale structures during formation of first stars, and (iii) Dark matter physics and inflation.

At redshifts higher than $z = 300$ (frequencies < 5 MHz), the neutral hydrogen signal is expected to disappear because the early Universe was sufficiently dense, hence the hyperfine HI state was in equilibrium with the cosmic microwave background due to residual ionization and collisions. [19] Hence a maximum wavelength of 100 m (minimum frequency of 3 MHz) is appropriate for LCRT.

Galactic Foreground Noise —One of the main challenges in collecting data at such low frequencies is the synchrotron radiation from our own Milky Way galaxy, referred to as the Galactic foreground. This foreground is five orders of magnitude stronger than the Dark Ages signal in the LCRT band, as shown in Fig. 7. However, we know the spatial structure, spectral shape, and polarization of the Galactic foreground signal. We will use these properties to separate the strong Galactic foreground signal from the weak Dark Ages signal.

Fig. 8 shows the Galactic foreground signal in the Galactic reference frame. The lines show the region of the sky that LCRT would see, with appropriate beam-width and no steering, if it were located at different latitudes on the Moon. We would like to avoid the strong signals from the center of
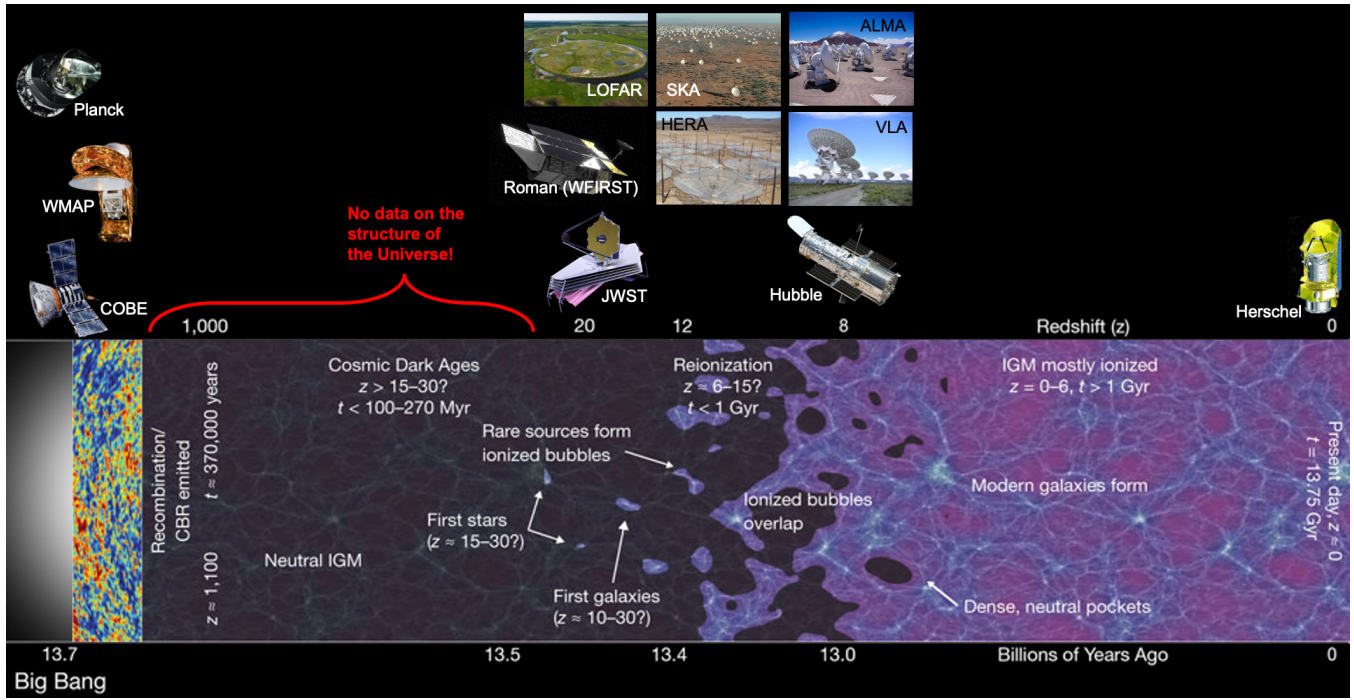
Figure 5: Evolution of the Universe (adapted from Ref. [18]). Also shows the spacecraft and ground telescopes collecting data at different redshifts.
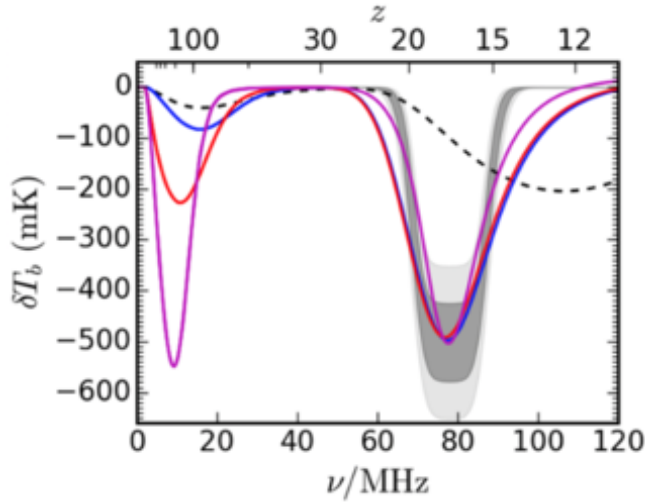

Figure 6: Signals from Dark Ages and First Stars "Cosmic Dawn" (image credit: [25])

Figure 7: Galactic foreground is 5 orders of magnitude stronger than the Dark Ages signal (image credit: [27])

the Milky Way Galaxy, while also covering different sections of the sky. We hence choose to select lunar craters near $20°$N latitude.

In terms of longitude, the ideal location for LCRT would be close to the $180°$ longitude to minimize the likelihood of interference from terrestrial RF sources. This is illustrated by Fig. 9 from Ref. [28] which shows simulation results at 30 kHz describing how RFI incident from the left is attenuated behind the Moon on the right. The dispersion of the signal is higher at 30 kHz, which is two orders of magnitude lower than the lowest target frequency of LCRT i.e. 3 MHz. Hence, LCRT is less sensitive to the longitudinal
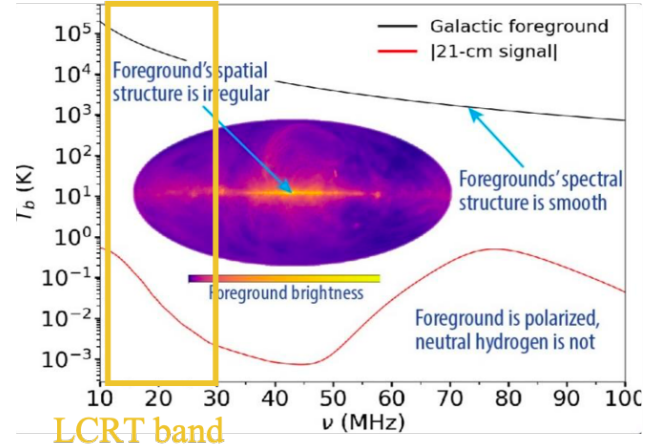
location than what is indicated by this figure. But in general, this figure illustrates clearly, the importance of placing the lunar telescope on the far side of the moon for shielding from terrestrial noise sources.

Solar System Noise Sources —Detection of radio emission at 22 MHz from Jupiter was identified quickly as being due to its planetary-scale magnetic field [29], [30]. Subsequent spacecraft investigations have revealed that many of the planets, and even some moons, either have or have had a planetary-scale magnetic field. The emission process is due to accelerated electrons streaming down the planet's magnetic field toward its magnetic poles. All "magnetic" planets show a sharp truncation in their radiated powers at an upper
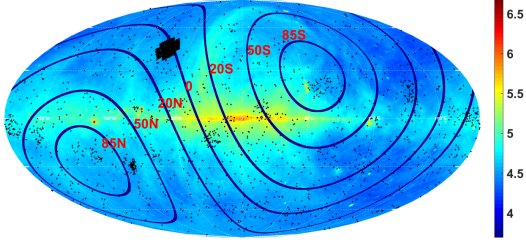
Figure 8: Galactic foreground as a function of Lunar latitude, with known Exoplanets
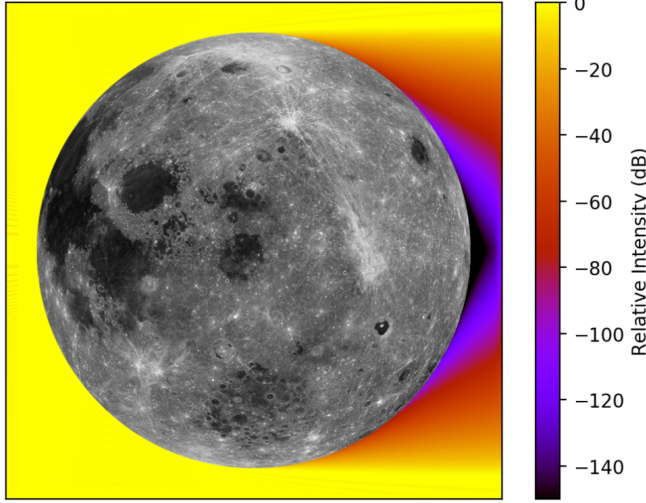

Figure 9: Simulation results at 30 kHz showing how RFI incident from the left is attenuated behind the Moon on the right (image credit: [28])
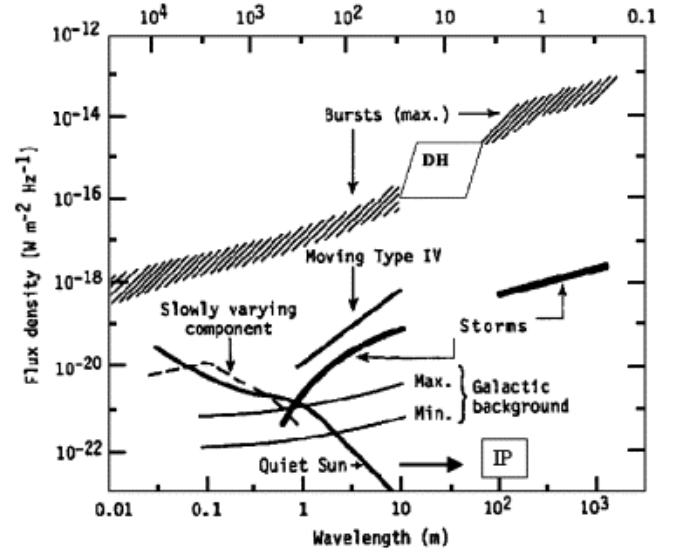

Figure 10: Schematic diagram showing the flux densities of various radio phenomena 0.01 m to >1 km. In the top, the corresponding frequencies are marked in MHz. The gap between 10 and 100 m (decameter to hectometer wavelengths, or DH for short) was due to the wavelengths employed by ground-based and space-based radio observations. This gap was filled by the launch of Wind/WAVES experiment as indicated by the parallelogram "DH". Radio emission at wavelengths longer than 10 m are considered interplanetary (IP). The flux density of types II and III radio bursts is the largest at all wavelengths, as marked by 'Bursts (max.)'. The maximum and minimum observed flux densities of the Galactic background are also shown. The Galactic background rises a bit more and peaks around 100 m with a flux density of 10^{-9} W m^{-2} Hz^{-1}. The quiet Sun emission falls below the Galactic background, but the type III storms and interplanetary radio bursts of types III and IV are much brighter than the Galactic background. (Reproduced from [31])

frequency determined by where the local cyclotron frequency (determined by the strength of the planet's magnetic field) drops below the local plasma frequency (determined by the atmospheric density). For Jupiter, this cutoff frequency is near 40 MHz.

The Sun is also a strong noise source in these wavelengths, especially during coronal mass ejections [32], as shown in Fig. 10. A number of single dipole measurements have been carried out by the following instruments:

- WAVES instrument on the Wind spacecraft [33]
- S/WAVES instrument on the STEREO mission [34]

Due to their poor angular resolution, these instruments had essentially no sensitivity to astronomical sources outside of the solar system.

Technical Requirements of LCRT for Satisfying Science Objectives — As mentioned in Section Galactic Foreground Noise, the Galactic foreground is several orders of magnitude stronger than the signal of interest. Based on recent analyses presented by Rapetti et. al. [35], Tauscher et. al. [36] and Rao et. al. [37], the foreground removal process does not introduce a large systematic error in the synthesis of the 21-cm signal from simulated data. Therefore, first order estimates of the observation duration (τ) can be estimated

from the radiometer equation

$$\sigma = \frac{T_{sys}}{\sqrt{\Delta\nu\tau}} \tag{1}$$

where σ is the noise, and $\Delta\nu$ is the bandwidth of each frequency channel or the spectral resolution desired in the derived signal. T_{sys} is the sum of the radio sky temperature and the receiver noise temperature, which is dominated at LCRT wavelengths by the radio sky. For a system temperature of 10^5 K and $\Delta\nu$ of 1 MHz, the variation of noise as a function of integration time is shown in Fig. 11. This figure shows that with roughly half a year of observation time, we would reach noise levels close to 25 mK, which would satisfy the requirement outlined in Table 2.

A more detailed analysis along these lines was carried out by Rapetti et. al. [35]. The plots from their paper, reproduced in Fig. 12, show that as the duration of telescope operation increases, the uncertainty in our estimation of the absorption curve (Ref. Fig. 6)) decreases. Just 800 hours into the observation cycle, we can start deciphering the shape of the absorption profile and by the time we reach observation times close to half a year, we start narrowing the uncertainties
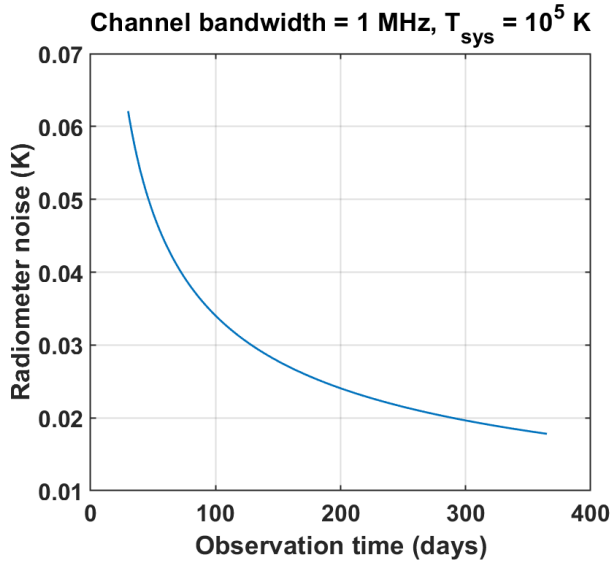
Figure 11: Variation of integrated noise temperature as a function of integration time, assuming a bandwidth of 1 MHz and system temperature of 10^5 K.

sufficiently to start distinguishing among the various models that predict the shape of the dark ages absorption trough.

LCRT's technical requirements and other parameters for achieving the above science objectives are shown in Table 2.

Parameter	LCRT's Value
Wavelength (Frequency) Range	$10 - 100$ m ($3 - 30$ MHz)
Location on Far-side	$\approx 20°$N and $180° \pm 45°$E
Mesh Diameter	≈ 1 km
Mesh Shape	Parabolic shape
Mesh Spacing	$1 - 2.5$ m
Angular resolution $\left(\theta_{res} \approx 1.22\frac{\lambda}{Dia}\right)$	Desired $\theta_{res} < 5°$ [38], Actual $\theta_{res} = 42'$ for $\lambda = 10$ m, $\theta_{res} = 3.5°$ for $\lambda = 50$ m, $\theta_{res} = 7°$ for $\lambda = 100$ m
Operational Life	1 year for desired SNR > 5
Preferred Observation Time	Lunar night

Table 2: LCRT's Technical Requirements for achieving its Science Objectives

Potentially Secondary Science Objectives of LCRT—In addition to the primary science objectives discussed above, LCRT could also potentially enable the following secondary science objectives.

Radio Emissions from Extrasolar Planets There is a long history of both predictions of and searches for extrasolar magnetospheric radio emissions [39], [40]. As discussed in Section Solar System Noise Sources, the radio emission process are due to accelerated electrons streaming down the planet's magnetic field toward its magnetic poles. Generated by dynamo processes within the planet, planetary-scale magnetic field are a remote-sensing method to constrain the properties of a planet's interior, and it may be possible to measure the magnetic fields of extrasolar planets. If this proves
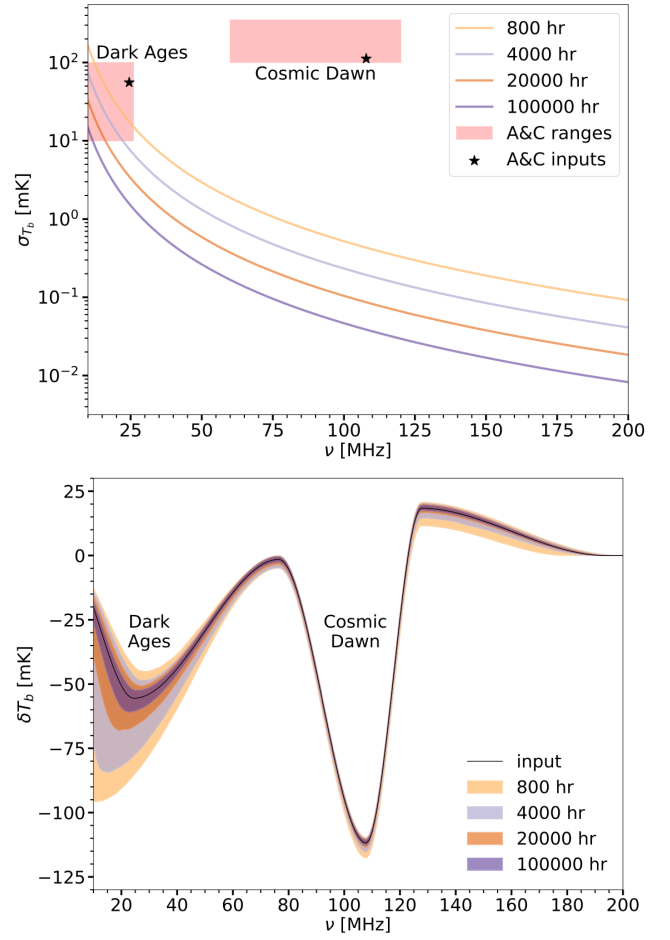

Figure 12: *(top)* 1σ noise levels for different integration times at different frequencies. The red boxes and the black stars within them represent estimates of the ranges of temperatures and frequencies corresponding to the signals from the Dark Ages and Cosmic Dawn.
(bottom) Estimates of total uncertainty in reconstruction of the 21-cm signal for different integration times. (Image credit: [35])

possible, it will offer one of the few means of understanding the potential diversity of planetary interiors. In the case of the Earth, its magnetic field has also been speculated to be partially responsible for its habitability. Thus, knowledge of the magnetic field of an extrasolar planet may be a necessary component of assessing its habitability, or understanding an absence of life on an otherwise potentially habitable planet. All of the giant planets in the solar system and the Earth generate radio emission via the electron cyclotron maser instability, which results from an interaction between the solar wind and the planetary magnetosphere.

The LCRT's beam might serendipitously pass across some of the known extrasolar planets, as shown in Fig. 8, and LCRT might be able to observe these radio emissions. LCRT won't have the necessary angular resolution to resolve these targets.

Extend LCRT's Wavelength/Frequency Range It might be possible to increase LCRT's wavelength (frequency) range to include the 1–5 m wavelength band (i.e., 30–150 MHz frequency band) with an upgrade to the reflector's design and an additional set of receivers for these frequencies. The high-
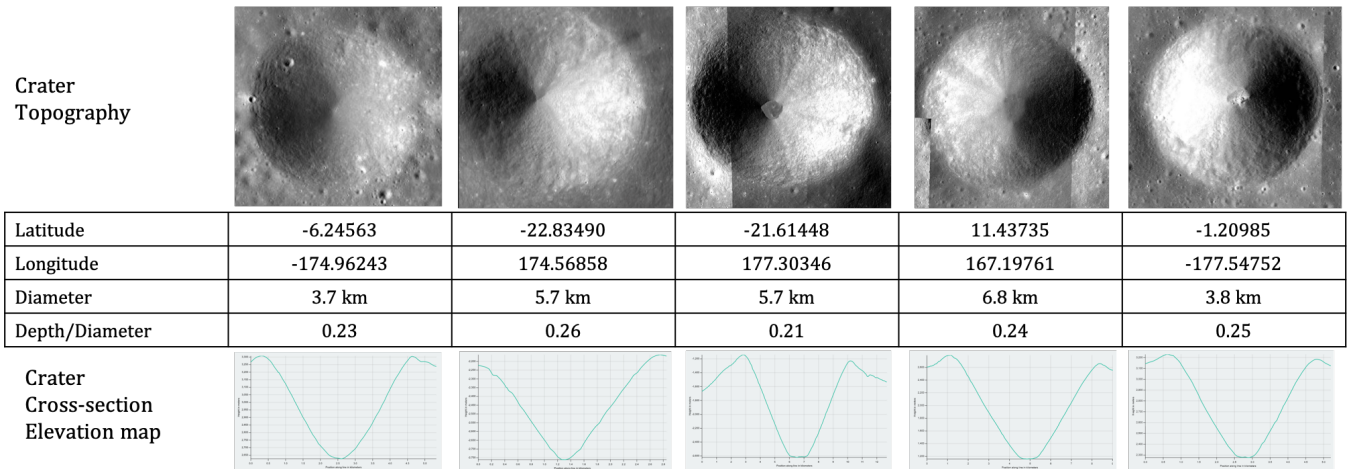
Crater Topography					
Latitude	-6.24563	-22.83490	-21.61448	11.43735	-1.20985
Longitude	-174.96243	174.56858	177.30346	167.19761	-177.54752
Diameter	3.7 km	5.7 km	5.7 km	6.8 km	3.8 km
Depth/Diameter	0.23	0.26	0.21	0.24	0.25
Crater Cross-section Elevation map					

Figure 13: Five potential lunar-craters for LCRT

density mesh could be added only to the sections closer to the center, thereby not incurring a massive weight penalty.

This would open the door to calibrating LCRT using observations of the same astronomical sources that are visible from Earth and further refine the ionospheric models that are the main limiting factor in conducting observations from Earth in these frequency bands. For example, the EDGES data [24], [26] shown in Fig. 6 has come under considerable scrutiny due to their ionospheric corrections.

Finally, this would also enable very large baseline interferometry (VLBI) between LCRT and Earth-based radio telescopes. This might open to door to high-resolution imagery of first stars and early galaxies in these ultra-long wavelength bands.
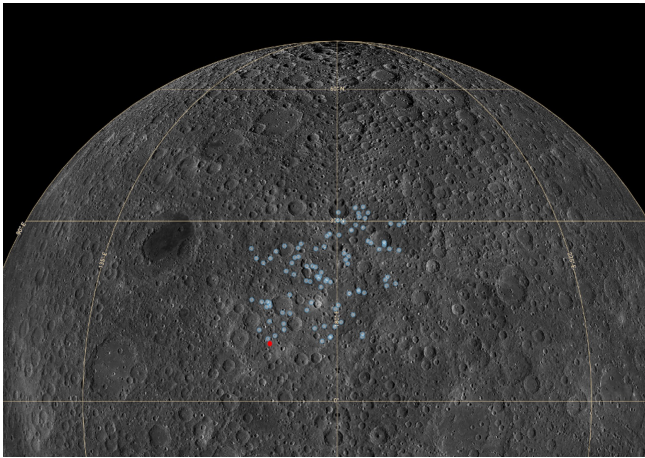
3. LUNAR CRATER SELECTION

Figure 14: 50 candidate craters for LCRT. Selected crater is shown in red.

The Lunar Reconnaissance Orbiter (LRO) mission has generated high-resolution imagery of the Moon. In the LRO Camera database [41], there are over 82,000 craters in the 3-5km diameter range that are excellent candidate craters for LCRT. Some examples are shown in Fig. 13. The key requirements on the crater are:

- Diameter range within 3-5 km
- Minimum crater depth of 600 m, so that both reflector and feed are suspended inside the crater.
- Location on farside near $\approx 20°$N and $180° \pm 45°$E to avoid Earth-based radio interference near the lunar limbs.
- No boulders or outcrops, that could cause difficulty while deploying the reflector
- Complete crater rim for uniform deployment of lift wires and anchors along all directions.
- Level surface and gentle slope outside the crater as these could serve as potential landing site or operations sites outside the crater.

We manually surveyed $\approx$300 craters to check for the above desired characteristics. Fig. 14 shows 50 candidate craters that were thoroughly analysed. The best crater is shown in Fig. 15a, Fig. 15b, and it has the following parameters:

- Location: $9.29553°$N Latitude, $169.07779°$E Longitude
- Diameter: 3.82 Km
- Depth: 960 m
- Depth to diameter (d/D) ratio: 0.251

This crater has a high d/D ratio, with a relatively small diameter. Such a high d/D ratio is usually seen in much larger craters [41]. Additionally, this crater has a flat and continuous rim, uniform circular shape, uniform crater walls on all directions, and no boulders or outcrops. The slope of the crater shown in Fig. 15c, both inside and outside was analyzed, to confirm that our robots could easily operate there.

4. REFLECTOR WIRE MESH DESIGN

The wire mesh that forms the parabolic-shaped reflecting dish is composed of radial wires (that run from the central lander at the crater floor to the crater rim) and circumferential wires (that electrically connect neighboring radial wires). The radial wires are the main load-bearing wires that determine the shape of the reflecting dish. The circumferential wires are small, light-weight and freely move over the radial wires.
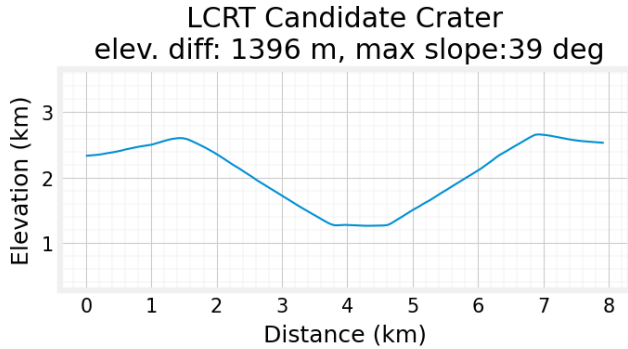
The LCRT reflector has a complex design, since its key component dimensions span six orders of magnitude, i.e the reflector is 1km in diameter while the wires used in the mesh are 1mm in diameter. We conducted multiple studies to
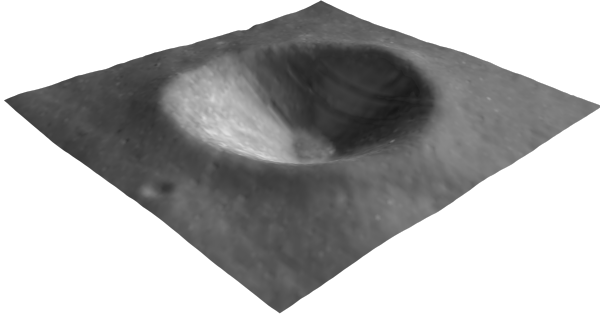
(a) Depth Elevation Map (DEM)
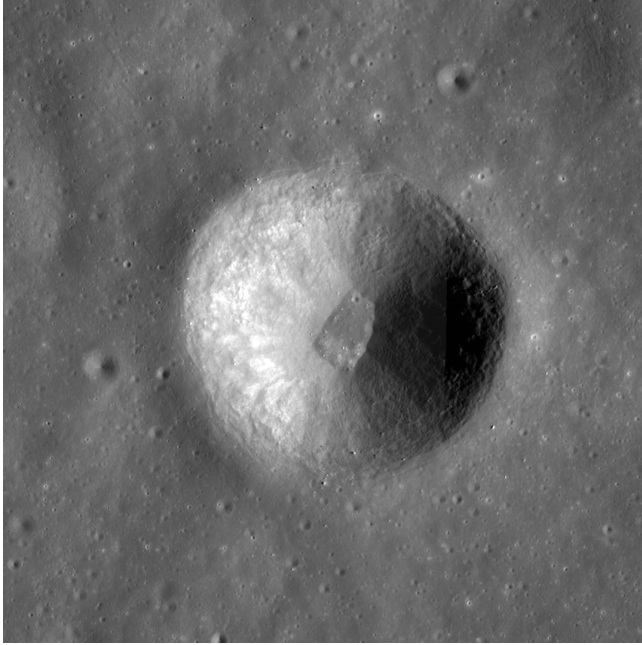
(b) High-resolution image

(c) Side profile and slope of the selected crater

Figure 15: LCRT's selected crater at $9.29553°$N and $169.07779°$E

separately prove the feasibility of the following factors:

1. We studied the problem of storage and deployment of a large 1km diameter reflector from a lunar lander
2. We analysed the structural and thermal loading on the reflector during deployment and nominal operations on the Moon
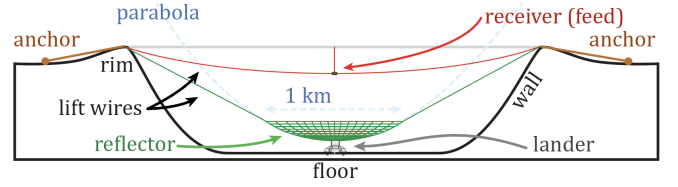

Figure 16: Cross-Section view of LCRT (not to scale)

3. We analysed the radio performance of the reflector to understand its characteristics

The objective of these studies was to show that a feasible path forward exists. Future work will focus on the design of a mesh that simultaneously satisfies inter-disciplinary constraints combining all the factors discussed above.

Linear-Density Profile for Parabolic Shape

The linear-density (i.e., thickness/mass variation) of the wires is designed such that the shape of the freely hanging wire mesh, anchored only at the crater floor and crater rim, conforms to the desired parabolic arc with 2 m accuracy (instead of a catenary shape) (Fig. 16) [42]. Since the linear density does not change due to thermal variations, the wire-mesh passively maintains its shape across large thermal fluctuations ($100°$C to $-173°$C) over a lunar day. We now mathematically derive this linear-density (i.e., thickness/mass variation) of the radial and circumferential wires.
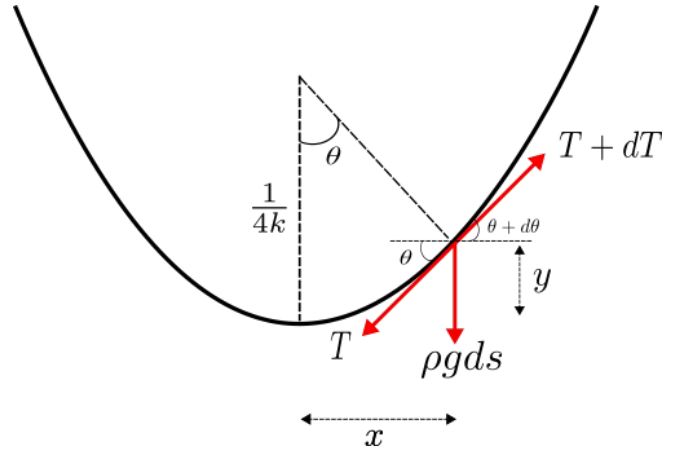

Figure 17: Force diagram for a small element of a wire suspended from two fixed points, where the parabola is defined by $y = kx^2$

As shown in Fig. 17, by balancing the forces acting on a small element of length ds, we arrive at the following equations

$$dT = \rho g ds \sin \theta \qquad (2)$$
$$T d\theta = \rho g ds \cos \theta \qquad (3)$$

For a parabola described by $y = kx^2$, we have

8

$$dy = 2kxdx \tag{4}$$

$$ds = \sqrt{dx^2 + dy^2} \tag{5}$$

$$\Rightarrow ds = dx\sqrt{1 + 4k^2x^2} \tag{6}$$

From Fig. 17, we also have

$$\tan\theta = \frac{x}{\frac{1}{4k} - y} \tag{7}$$

Differentiating on both sides, we get

$$\sec^2\theta d\theta = \frac{\left(\frac{1}{4k} - y\right)dx + xdy}{\left(\frac{1}{4k} - y\right)^2} \tag{8}$$

$$= \frac{\left(\frac{1}{4k} - y\right)dx + 2kx^2dx}{\left(\frac{1}{4k} - y\right)^2} \tag{9}$$

$$= \frac{\left(\frac{1}{4k} - kx^2 + 2kx^2\right)dx}{\left(\frac{1}{4k} - y\right)^2} \tag{10}$$

$$= \frac{\left(\frac{1}{4k} + kx^2\right)ds}{\left(\frac{1}{4k} - y\right)^2\sqrt{1 + 4k^2x^2}} \tag{11}$$

Using Equations 2 and 3, we get

$$\frac{dT}{T} = \tan\theta d\theta \tag{12}$$

Integrating this equation gives

$$T = \frac{T_0}{\cos\theta} \tag{13}$$

Using this in Equation 3 gives

$$\frac{T_0}{\rho g} = \frac{ds}{d\theta}\cos^2\theta \tag{14}$$

Now using Equation 11, we get

$$\frac{T_0}{\rho g} = \frac{\left(1 - 4k^2x^2\right)^2}{4k\sqrt{1 + 4k^2x^2}} \tag{15}$$

$$\Rightarrow \rho = \frac{T_0}{g}\frac{4k\sqrt{1 + 4k^2x^2}}{\left(1 - 4k^2x^2\right)^2} \tag{16}$$

$$= \rho_0\frac{\sqrt{1 + 4k^2x^2}}{\left(1 - 4k^2x^2\right)^2} \tag{17}$$

In terms of focal length f, this equation becomes

$$\frac{\rho}{\rho_0} = 8f^3\frac{\sqrt{4f^2 + x^2}}{\left(4f^2 - x^2\right)^2} \tag{18}$$

The number of radial wires needed to maintain a spacing of $\lambda/4$ increases with θ, and hence x. Let $N(x)$ represent
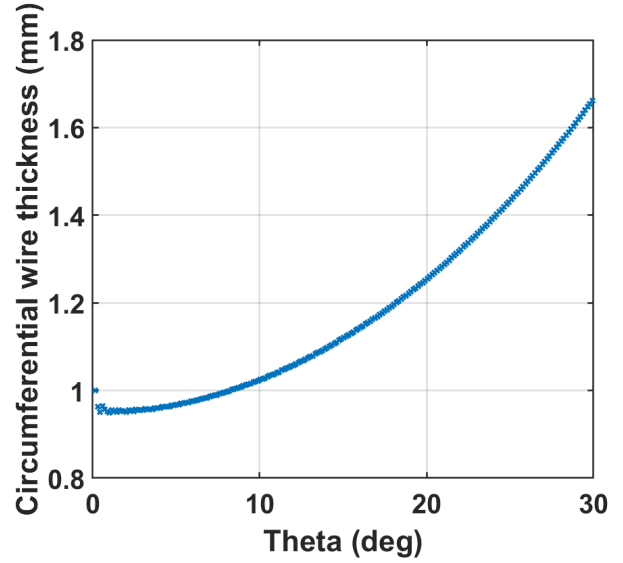

Figure 18: Variation of thickness of circumferential wires as we move away from the bottom of the crater.

the number of radial wires at x. We assume that each wire has constant linear mass density but the effect of variable linear mass density, as defined by Equation 18, is achieved by varying the thickness of the circumferential wires. In fact, each radial wire is assumed to have the same thickness t_0 as the first circumferential wire. The effective ratio of linear mass density (ρ) at x and ρ_0, taking into account the loading due to circumferential wires, can now be computed as

$$\frac{\rho}{\rho_0} = \frac{\frac{2\pi xt^2}{N(x)} + \frac{\lambda}{4}t_0^2}{\frac{2\pi x_1 t_0^2}{N_0} + \frac{\lambda}{4}t_0^2} \tag{19}$$

where, x_1 is the radius of first circumferential wire and N_0 is the number of radial wires at the lowest point on the mesh. We can now combine Equations 18 and 19 to calculate the variation of thickness of circumferential wires. This variation is plotted in Fig. 18.

There would be a total of 210 circumferential wires in the mesh, assuming a radius of 500 m and $\lambda/4$ spacing. The minimum number of radial wires needed to maintain $\lambda/4$ spacing in each circumferential zone (between two adjacent circumferential wires) is plotted in Fig. 19. While using the minimum number of radial wires will lead to a mesh with the minimum possible mass, discontinuities in the radial wires will not be ideal from a structural perspective. In addition, the analytical derivation for a single wire discussed earlier in this section is less likely to hold for a mesh made up of discontinuous radial elements. Therefore, we adopt a tiered approach where the number of radial wires increases at regular intervals, as illustrated with two tiers for a 100 m mesh in Fig. 20. The actual number of radial wires in most cases will therefore be slightly higher than the minimum value shown in Fig. 19.

The wire mesh will have the design shown in Fig. 20 to ensure wire spacing $\leq \min(\lambda)/4$, where each radial wire has resistance less than 10Ω to enable efficient radio reflection [40]. The corresponding design for LCRT's 1km-reflector's mesh is shown in Fig. 21. Note the complexity in designing and
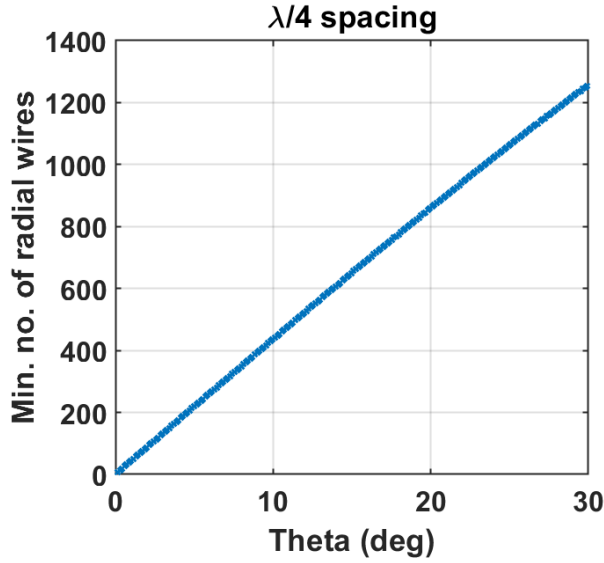
Figure 19: Number of radial wires in each circumferential zone (between two adjacent circumferential wires) as we move radially outwards, assuming $\lambda/4$ spacing.
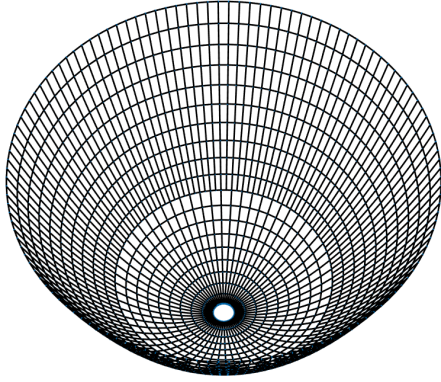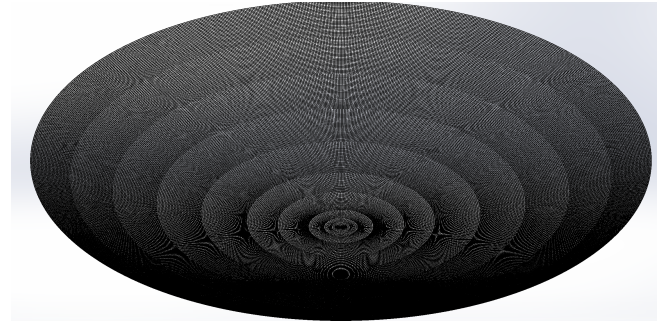

(a) Zoomed out view to show the entire mesh

(b) Zoomed in view

Figure 21: LCRT 1km-reflector's mesh design

Figure 20: An illustration of tiered increase in the number of radial wires while maintaining wire spacing $\leq \min(\lambda)/4$ for a 100 m mesh.
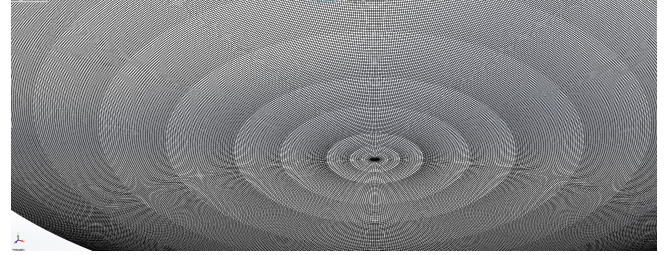
analysing this mesh, whose key components span six orders of magnitude.

Micro-meteoroid Impact Risk

One of the several mission risks that LCRT has to deal with is the threat from meteoroid impacts. Since the reflector mesh is made up a large number of interconnected wires, the severance of a few of those wires will not have any significant detrimental impact on the mechanical or electromagnetic performance of the mesh. The bigger risk is the likelihood of an impact event cutting one of the sixteen lift wires holding up the reflector or one of the four lift wires holding up the feed. These wires are assumed to be 1 mm in thickness. To carry out an approximate estimate of the impact probability, we assume that a particle which creates a crater of diameter greater than 1 mm on impacting an aluminum plate is going to definitely cut the lift wires upon impact. The flux of such particles for the lunar environment can be obtained from the plot in Fig. 22 reproduced from Vanzani et al. [43]. This figure shows that the cumulative flux density corresponding

Figure 22: Cumulative density flux of impact events as a function of the impact-crater diameter created upon impact on an aluminum plate on the lunar surface. (Image credit [43])

to this damage threshold is $0.08 \text{ m}^{-2} \text{ yr}^{-1}$. The flux itself can now be estimated by multiplying this estimate with the cross sectional area of the lift wires. Twenty 1 mm thick wires, with each being roughly 1 km long, gives us a total impact area of 20 m^2. This translates to a flux of 1.6 wire-cutting impact events per year.

In order to overcome this risk, we propose using designs and weave patterns with in-build redundancy, such as the one shown in Fig. 23 proposed by Hoyt and Forward [44].

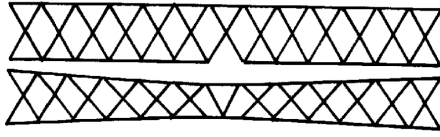**Figure 23**: A failure resistant design for a tether showing a single cut in the system. (Image credit [44]). The general idea is to create redundancy by replacing the individual lift wires with a redundant system of wires.

Finite Element Analysis (FEA) for Structural and Thermal Loading

The proposed mesh design is simulated using a high fidelity Abaqus FEA model at a sub scale of 50 m diameter and the deflection under gravity and thermal loading is computed. Abaqus scripting interface is used to import the complex mesh structure, as shown in Fig. 24. This process is also used to import origami structures to simulate deployment as explained later in the paper. Each cable is modeled as an aluminum beam with the thickness variations computed in Section Linear-Density Profile for Parabolic Shape. Each beam is connected to its neighbors with weld connectors, as shown in Fig. 25.
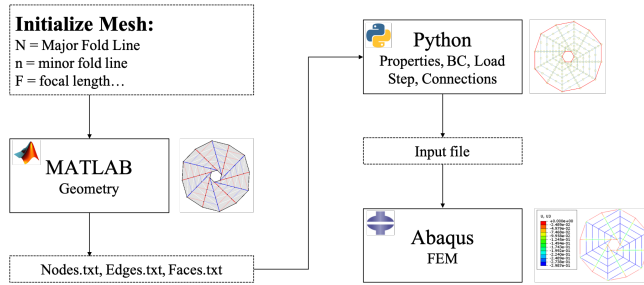

Figure 24: Developed FEA process to import the complex mesh structures from Matlab into Abaqus

- 3 connector elements
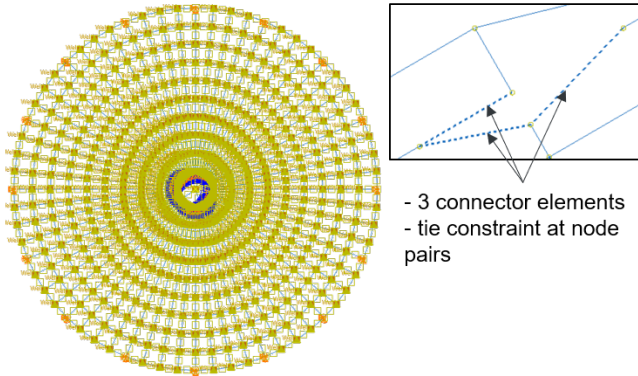- tie constraint at node pairs

Figure 25: Details of the Abaqus FEA model showing every beam, weld connection and the boundary condition

Since LCRT only operates during the lunar night (see Table 2), we analyze the thermal loading for the temperature gradient that LCRT will experience during the lunar night. It follows from Fig. 26 that LCRT will only experience temperature change (ΔT) of only 10 K during its operations at lunar night. Therefore, the mesh has to maintain its parabolic shape only over the 10 K ΔT variation during the lunar night.
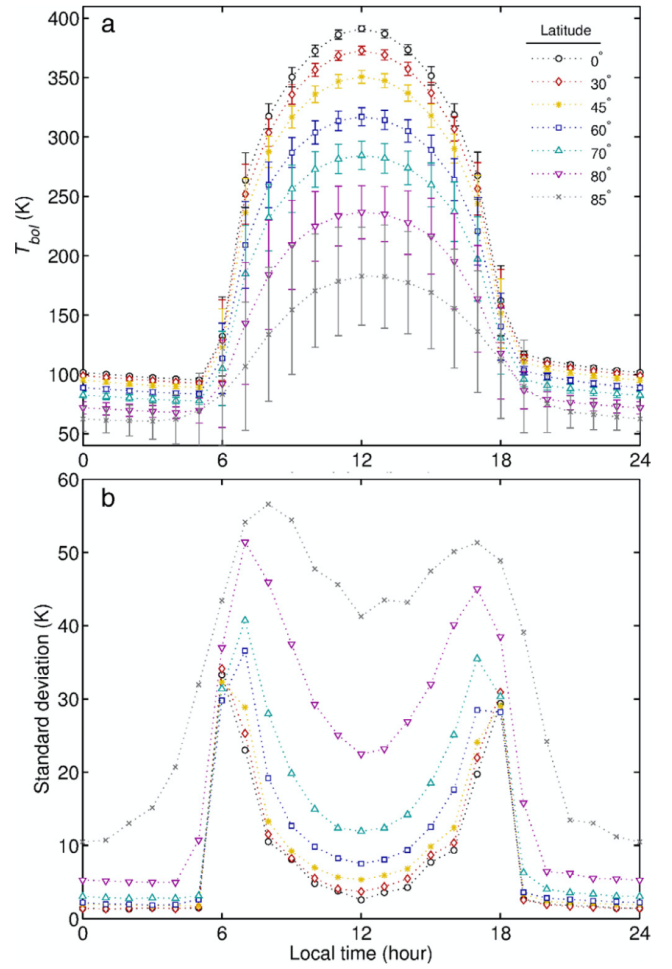
Figure 26: (a) Zonal mean bolometric temperatures and (b) standard deviation versus local time for latitude bands $0°$, $30°$, $45°$, $60°$, $70°$, $80°$, and $85°$; measured by the Diviner Lunar Radiometer Experiment onboard the Lunar Reconnaissance Orbiter (Reproduced from [45])
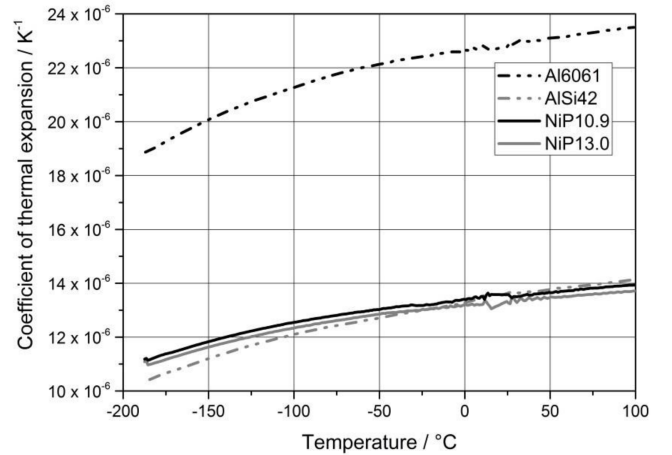
Figure 27: Coefficient of Thermal Expansion (CTE) of Al6061 in a temperature range from $-185°C$ to $100°C$. (Reproduced from [46])

Note that the mesh has to structurally *survive* temperature

changes over 200 K ΔT, but the shape does not have to conform to that of a parabola. Future work will show FEA analysis that the mesh can indeed structurally *survive* these large temperature changes.

Aluminium's Coefficient of Thermal Expansion (CTE) at 100 K is around 19×10^{-6} K^{-1}, and it varies slightly with temperature as shown in Fig. 27. In order to introduce some margin, we use CTE of 24×10^{-6} K^{-1} in our analysis.

$$Ft = Ft_y/\sin(\theta), \text{ where } Ft_y = mg/wires$$

(a) $y = x$

(b) Receiver Lift Wire Tension

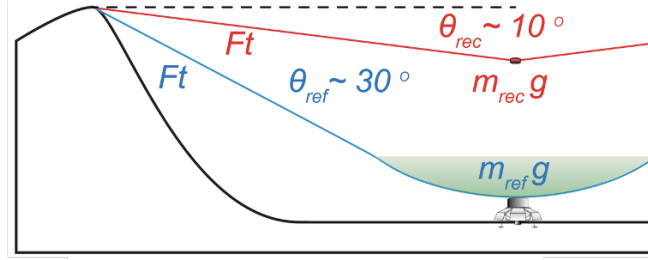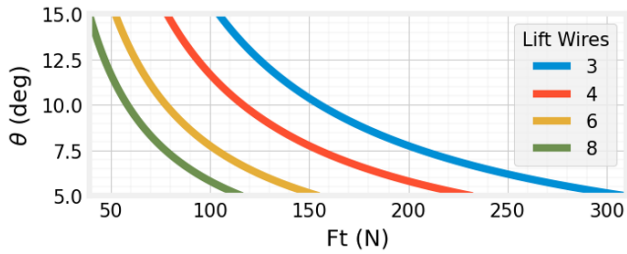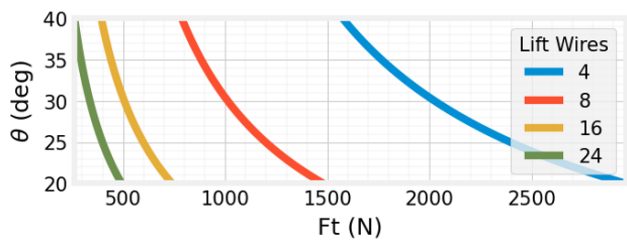(c) Reflector Lift Wire Tension

Figure 28: Calculation of number of Lift Wires

Assuming the receiver weighing 40 kg is deployed at $10°$ angle and the reflector weighing 2000 kg is deployed at $30°$ angle, the wire tensions in the lift wires are shown in Fig. 28. In order to limit the wire tension to 100-1000 N per anchor on the lunar surface, we need 4 lift wires for the receiver and 16 lift wires for the reflector.

Therefore, the reflector is held along the inner edge and on 16 points of the outer edge. The simulation runs in three geometrically nonlinear steps. First a small out of plan displacement is imposed to deform the structure from the original low stiffness shape and improve the convergence. Then gravity is applied in a quasi static step and finally temperature is increased by 10 K using a predefined field. Fig. 29 shows the vertical component of the final deflection. As expected the deflection of the anchored radial wires is small but it increases as we circumferentially move away from them. The maximum deflection is about 80 cm. In order to mitigate this large deflection as we scale up the structure, a

pretension in the cable could be applied.
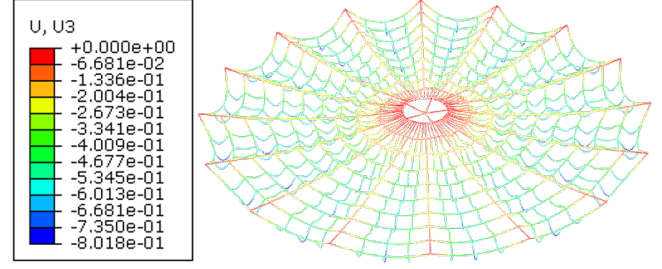
Figure 29: Vertical deflection (scaled by 4, U3 is in meters) of the 50 m mesh structure under Moon gravity ($1.62 \ m.s^{-2}$) and thermal loading ($\Delta T = 10$ K), when held along the inner edge and on 16 points of the outer edge.
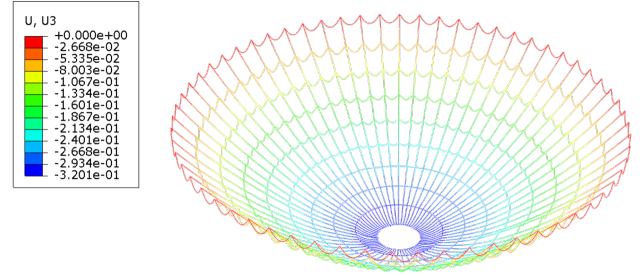
Figure 30: Vertical deflection (scaled by 50, U3 is in meters) of the 50 m mesh structure under Moon gravity ($1.62 \ m.s^{-2}$) and thermal loading ($\Delta T = 10$ K), when held along all points of the outer edge only.

For comparison, the deflection of the reflector held along all points of the outer edge is shown in Fig. 30.

Radio Frequency (RF) Performance of the Reflector
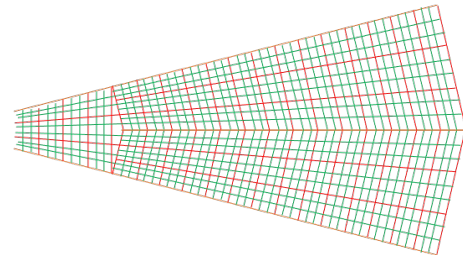
Figure 31: Wire mesh example used for RF analysis

	3 MHz	6 MHz	10 MHz	20 MHz	30 MHz
Ideal reflector	28.7	34.7	39.2	45.2	48.7
Gap of 1m	28.7	34.6	38.7	43.6	45.7
Gap of 2m	28.5	34.0	37.3	40.1	40.9

Figure 32: RF gain (measured in dBi) with reduced mesh spacing for 1-km diameter reflector

The 1km-reflector's RF performance was evaluated, assuming an ideal feed design (i.e. edge taper of -12dB at 64 degree, which is equivalent to a gain of 9.9dBi). The radiation pattern across different frequencies is shown in Fig. 33. The wire mesh example shown in Fig. 31 is assumed to have a wire-diameter of 2 mm, and the focal length of the 1km-diameter reflector is 0.4 km.
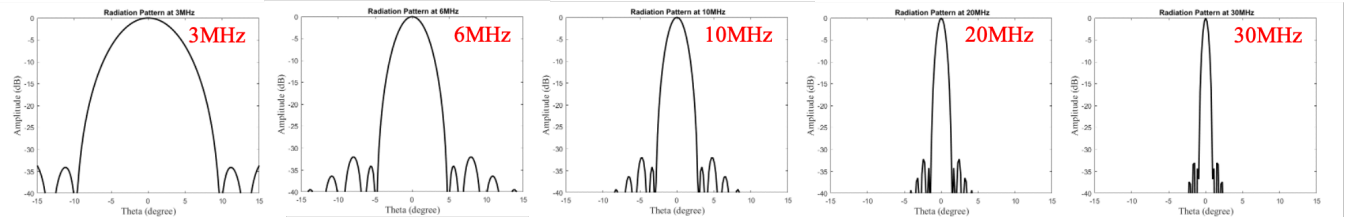
Figure 33: Radiation Pattern of the 1-km reflector at different frequencies

(a) 3 MHz   (b) 10 MHz   (c) 30 MHz
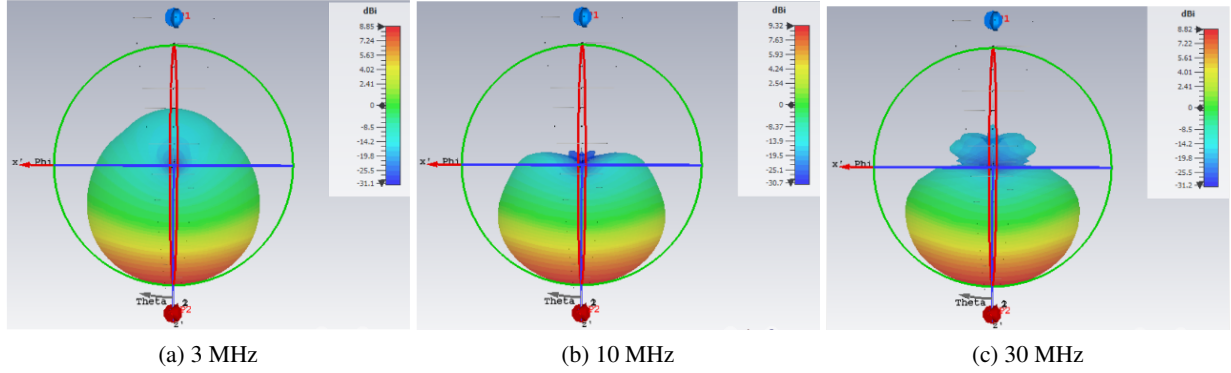
Figure 34: RF Performance of the Log Periodic Antenna (Feed) at different frequencies

The RF loss caused by reduced wire-spacing of 1m and 2m is shown in Fig. 32, where loss is the difference from the ideal reflector. On Earth, RF telescopes have mesh spacing $\approx$ min wavelength / 20 for near-ideal RF performance But this is not feasible for LCRT due to mass considerations. A mesh spacing ranging from $\lambda/10$ to $\lambda/4$ (1–2.5 m for $\lambda = 10$ m) does lead to a reduction in gain, but it can be compensated with longer observation time.
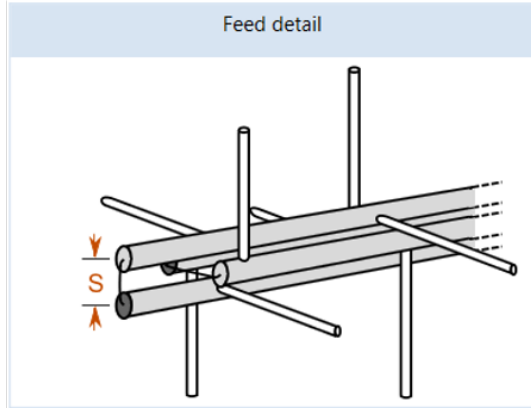
Figure 35: Log Periodic Antenna for LCRT (3D view)

Figure 36: Log Periodic Antenna for LCRT (Side view), with key dimensions

Radio Frequency (RF) Performance of the Feed

We selected a Log Periodic Antenna for LCRT, as it provides wide frequency band performance with stable gain and pattern. It also provides V, H, and C polarization. The overview of the Log Periodic Antenna is shown in Fig. 35–36, and it has a length of 150 m.

This feed has a gain of 8.5 dBi at 3MHz, and a gain of 9.5 dBi at 30 MHz. The performance of the feed at different frequencies is shown in Fig. 34. Future work will focus on reducing the feed dimensions to roughly 22m by 32m.

13

Method	Projectile w/ passive anchors	Rovers & passive anchors (dropped by rovers or landed separately)		Rovers as anchors
Rovers	**0**	**1**	**8**	**20** (1 per anchor)
Landers	LCRT & Deployment = **1**	1 LCRT + 1 Deployment = **2**	1 LCRT + 4 Deployment = **5**	1 LCRT + 10 Deployment = **11**
Deploy Time†	**< 1** Earth day	**74** Earth days	**9** Earth days	**4** Earth days
Redundant	**Yes**	**None**	**Yes**	**Yes**
Robustness	challenging to model/test, high terrain dependance, low heritage	none if primary rover fails, must survive the lunar night	minimum amount of rovers to deploy in a single lunar day	possible for extra rovers to retrieve lift wires for failed rovers
Landed Mass	20 projectile anchors = **2 mT**	1 rover + 20 anchor = **0.3+2 mT**	8 rover + 20 anchor = **2.6+2 mT**	20 rover = **6.5 mT**
Deploy Cost*	1 lander + 20 projectile^ = **$150+10 M**	2 lander + 1 rover = **$300+200 M**	5 lander + 8 rover** = **$750+800 M**	11 lander + 20 rover** = **$2+2 B**
Total Cost	deploy + antenna^^ = **$760 M**	deploy + antenna^^ = **$1 B**	deploy + antenna^^ = **$2.1 B**	deploy + antenna^^ = **$4.5 B**

† Time assumes 2 cm/s avg. velocity and deployment of 20 lift wires
* Lander includes launch vehicle ($50 M/launch, $100 M/lander)
** Rover cost ½ for multiple units
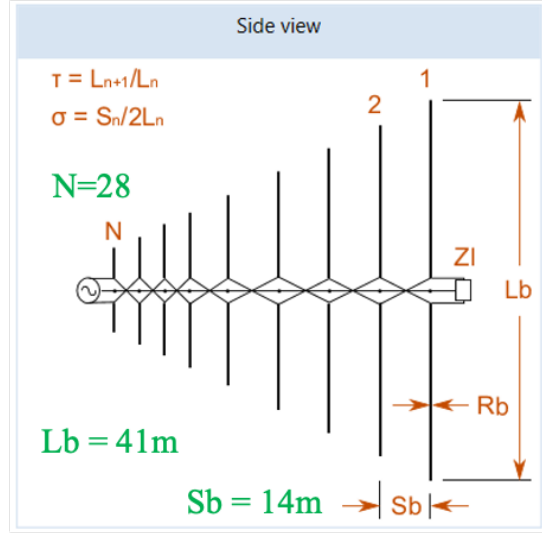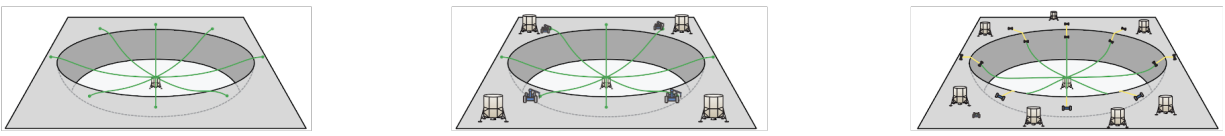^ Projectile anchor cost $1M/each
^^ Antenna system cost $ 500 M

Figure 37: Concept of Operations (ConOPs) Trade-space for LCRT
(*Disclaimer:* The cost information contained in this document is of a budgetary and planning nature and is intended for informational purposes only. It does not constitute a commitment on the part of JPL and/or Caltech.)

5. CONCEPT OF OPERATIONS
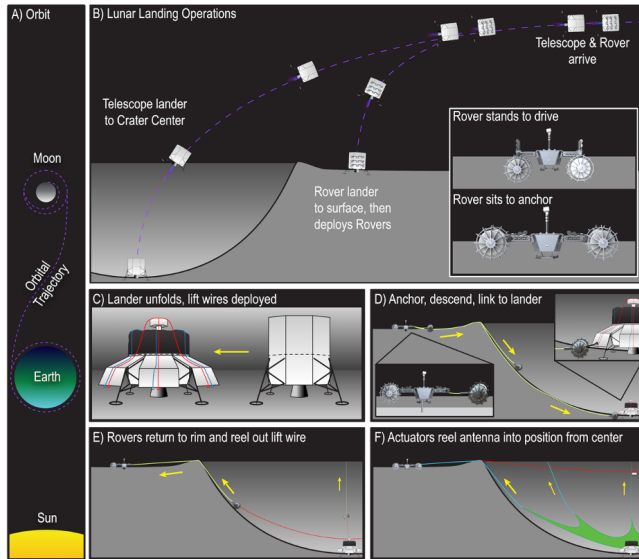
Figure 38: Concept of Operations for building LCRT, shows Phases **(A)**, . . . , **(F)**

The concept of operations (ConOPs) for constructing LCRT is shown in Fig. 38. **(A)** A spacecraft approaches the selected crater on the far-side of the Moon, carrying all the equipment necessary for constructing LCRT. **(B)** One half of the spacecraft lands in the crater floor, carrying the wire mesh and receiver antenna. The other half of the spacecraft lands on the crater rim, carrying the DuAxel robots and supporting equipment. The lander at the crater floor travels to the optimum position, then anchors itself and deploys guide wires. Multiple DuAxel robots rappel down the crater walls, link to the guide wires, hoist the receiver antenna, and deploy the wire mesh. These steps are discussed in detail as follows:

- **(C)** Antenna preparation and lift wires deployment. (See Section Packaging of Reflector)
- **(D)** DuAxel rovers anchor to the terrain. Axel rovers (See Fig. 39) descend and link to lift wires on lander. (See Section Tethered Rovers)
- **(E)** Rovers return to the crater rim and anchor the lift wires. (See Section Deploying Lift Wires and Anchoring Lift Wires)
- **(F)** Lift antenna components. (See Section Lifting Feed and Deploying Reflector and Finite Element Analysis (FEA) of Reflector Deployment)

Further details of the LCRT deployment process are presented in [47]. Next, LCRT is calibrated and using known radio sources [48] and it starts exploring the universe! Multiple steps in the construction process can be performed in parallel.

Figure 39: Axel and DuAxel rovers are being field-tesed for climbing steep terrains and cliff faces

An initial trade-space analysis in Fig. 37 shows that there is a wide variety of alternative ConOPs strategies, ranging from
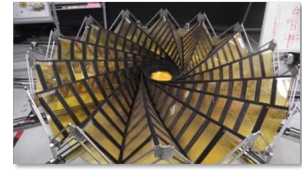
Configs	Folded	Support Ring	Origami
Detail	basic folding of wire mesh into a container, similar to commercial fishing nets	systematic folding with ring support structure	mesh wrapped around disc/mandrel with self-releasing constraints, pulled from edge
Example	n/a	ASTROmesh	Starshade
Requires	container	outer support ring	strain material built into mesh
Support	rim wires	rim wires + lander	rim wires + lander
Max size	100s m	10s of m	100s m (theoretically, current is 10 m)
Reliability	low	high	high

Figure 40: Comparison of reflector packaging strategies

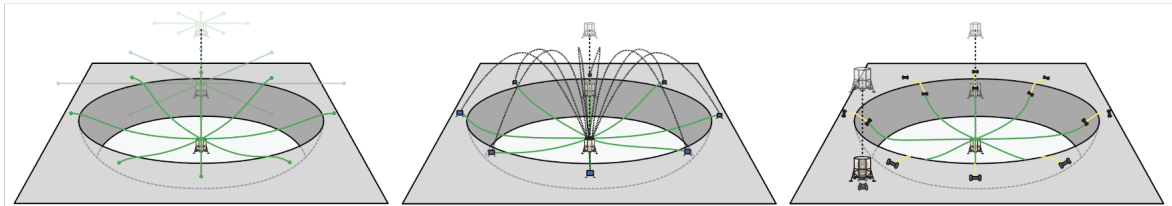| Configs	Top Down	Bottom Up	Hybrid
Detail	lander deploys lift wires during descent using mass ejection approach	lander deploys lift wires from crater floor using projectile or hopper	antenna components delivered to crater floor, anchors/deployers to rim
Anchoring	limited by mass, likely passive only	limited by mass/lift and lander volume	decouples anchoring & antenna deployment
Reliability	low	medium	high
Complexity	low	medium	high (two or more landers, multiple rovers)
Testability	low	medium	high

Figure 41: Comparison of top-down, bottom-up, and hybrid approaches to deploy lift wires

a single lander (moderate-risk mission) to multiple landers (low-risk mission). We envisage that LCRT will fall in the flagship-class missions category of NASA projects.

Packaging of Reflector

Some approaches are shown in Fig. 40. Structural integrity of the reflector is of key concern, hence we favor integrating rigidity for a robust deployment. An origami approach, inspired by Starshade [49], is desirable for its ability to deploy using a 'single' degree-of-freedom, i.e., pulling on the lift wires will cause the antenna to unfurl from a central disc.

Deploying Lift Wires

Some approaches are shown in Fig. 41. The most reliable and robust solution for a construction of this magnitude requires a hybrid approach. Further details of the hybrid approaches are shown in Fig. 42. Tethered rovers serving as anchors reduce risk and allow for on-the-fly reconfiguration.

Tethered Rovers

The different options for tethered rovers (like Axel and Du-Axel) are shown in Fig. 43. In order to reduce dragging on both the rover tether and lift wire a dual spool system is preferred.

15
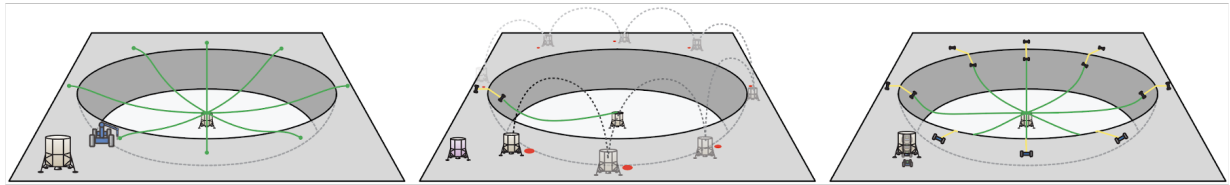
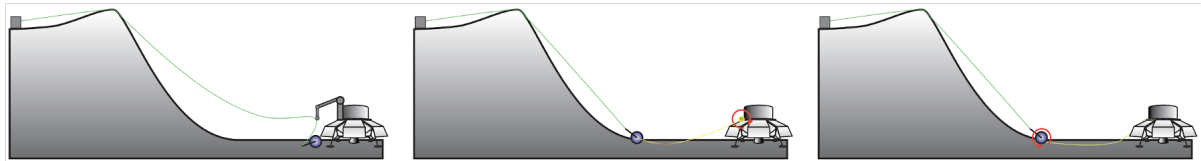| Configs	Tethered Projectiles + Rover	Tethered Rovers + Mass Anchors	Tethered Rovers Only
Detail	Projectiles with lift wires are launched to the rim, an anchoring rover is deployed around the rim to anchor each projectile to the terrain (likely using drill/stake)	Large, hopper lander delivers mass anchors around rim, tethered rovers arrive on separate lander and attached lander lift wires to mass anchors at rim	Tethered rovers serving as anchors or landers with attached rovers are deployed around the rim, rovers descend, and attach lift wires to the lander
Reliability	high terrain reliance, long-distance projectile req.	very good, reduces number of rovers needed	quasi-static, predictable, uses rover as anchor
Anchoring	requires rover to find each projectile and anchor	best anchor but difficult accommodate and drop off	enables many passive/active anchoring options
Complexity	projectiles launch complex, single or multiple rovers	complexity of mass drop-off high, multiple landings	one rover or lander per anchor
Mass	low, could be single rover used to set anchors	requires bringing dead multiple masses to surface	related to mass of rovers and landers needed

Figure 42: Further details of hybrid approaches to deploy lift wires

Configs	1-Way (single tether)	2-Way (rover tether, lander tether)	2-Way (dual rover tether)
Detail	rim anchored rover descends to lander, lander captures tether, lander loads tether onto internal spool to lift	rim anchored rover descends to lander, rover links to lander tether, rover ascends using 1st tether, 2nd payed out from lander	rim anchored rover descends to lander, rover links to lander, unspools a 2nd tether (within rover), 1st tether is used to ascend
Abrasion	limited on descent, some on reel in	limited on descent, dragged on ascent	limited throughout, managed on rover
Complexity	low for rover, complex handoff of tether	low for both rover and lander	more complex rover, two internal spools
Lift Wire	rover tether (heavy due to power/coms)	lightweight, high-strength fibers	lightweight, high-strength fibers

Figure 43: Comparison of different types of tethered rovers

Anchoring Lift Wires

Once deployed, the lift wires need to anchored at the crater rim. Some options are shown in Fig. 44. Ground-based rovers provide the most anchoring opportunities.

Additional details about these anchoring approaches are shown in Fig. 45. All highlighted anchor types are recommended for integration to the deployment rover.

Lifting Feed and Deploying Reflector

Once all the lift wires are in place, we need the lift the feed and deploy the reflector. Some options are shown in Fig. 46. Here 'Complexity' refers to control complexity to perform coordinated lift. We favor a centralized approach from power and control point of view, which also minimizes potential for damaging the lift wire due to abrasion on the lunar surface

and eliminates the need for thermal control of the lifting mechanism.

The lifting mechanism is inspired by cable-driven robot research and development, with the key difference that motors would be integrated into the lander. This mechanism is centrally powered and controlled by the lander.

Further details about LCRT deployment trade study are available at [47].

$$T_{\text{load}} = T_{\text{hold}}\, e^{\mu\phi}$$
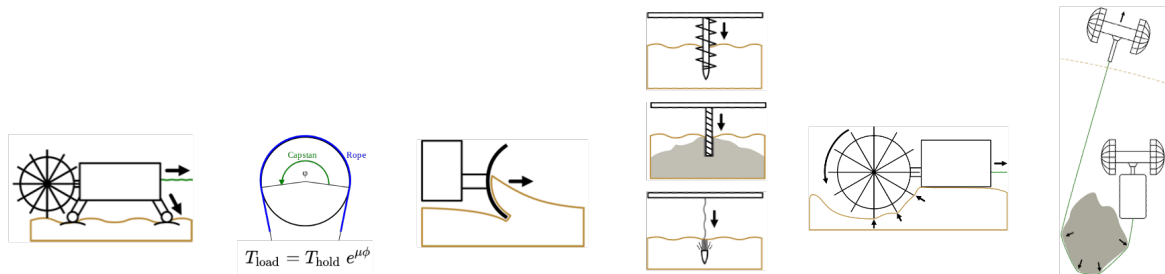
Anchors	Mass	Capstan Friction	Plow	Drill / Stake / Pyro	Excavation	Terrain Anchor
Detail	anchor resulting from mass resting on the surface (includes rover, lander, or projectile), less favorable on Moon	Lift wire on the surface generates a large holding force for a lesser applied force (see capstan equation)	Plow or wedge pushed into the soil leverages terramechanics, e.g., soil strength, to resist lift wire tension	Placed in soil or bedrock to anchor surface mass, depends on subsurface properties	Remove soil to bury anchor, e.g., beach sand anchors, requiring specialty hardware, e.g., backhoe	Use a large rock to wrap lift wire around, great anchor, not reliable or likely nearby crater (sparse dist.)
Projectiles	< 10 kg	Yes	Yes	No	No	No
Hoppers	10s of kg	Yes	Yes	Mass/Vol Limited	No	Yes, difficult flight
Rovers	100s of kg	Yes	Yes	Yes	Yes, difficult	Yes

Figure 44: Comparison of different anchoring options

Mass
> Example: Roof Anchor fall protection
> yields at 2.7 kN (0.3 ton)
> Resistance to slip or topple based on coulomb friction and attachment point

Ff = Fg*μ
Slip: Ft > Ff
Tip: Ft * y > Fg*(x/2)

Capstan Friction
> Coeff. of friction (μ) between sand and wire rope ~0.25
> Amplification of holding force occurs when the wire is in contact with the regolith due to capstan friction on sand and rocks

Ft anchor = Ft wire * e ^ (μφ)

Plow
> Example: PullPal sand anchor
> rated to 70 kN (8 ton)
> Plows in sand are used on rovers to minimize downhill slip

φ = soil shear strength
α = plow angle

Drill
> Apollo Lunar Surface Drill
> Cores: 3m x 2cm
> Rotary Percussive, ideal for low-preload drilling
> Drills leverage the soil strength, which on the moon (below 2 cm) is extremely compact with strong cohesion
> kN loads not likely an issue

Excavate
> Deadman Sand Anchor
> rated to 70 kN (8 ton)
> Most difficult robotically, requires removal of a significant amount of very dense lunar regolith material
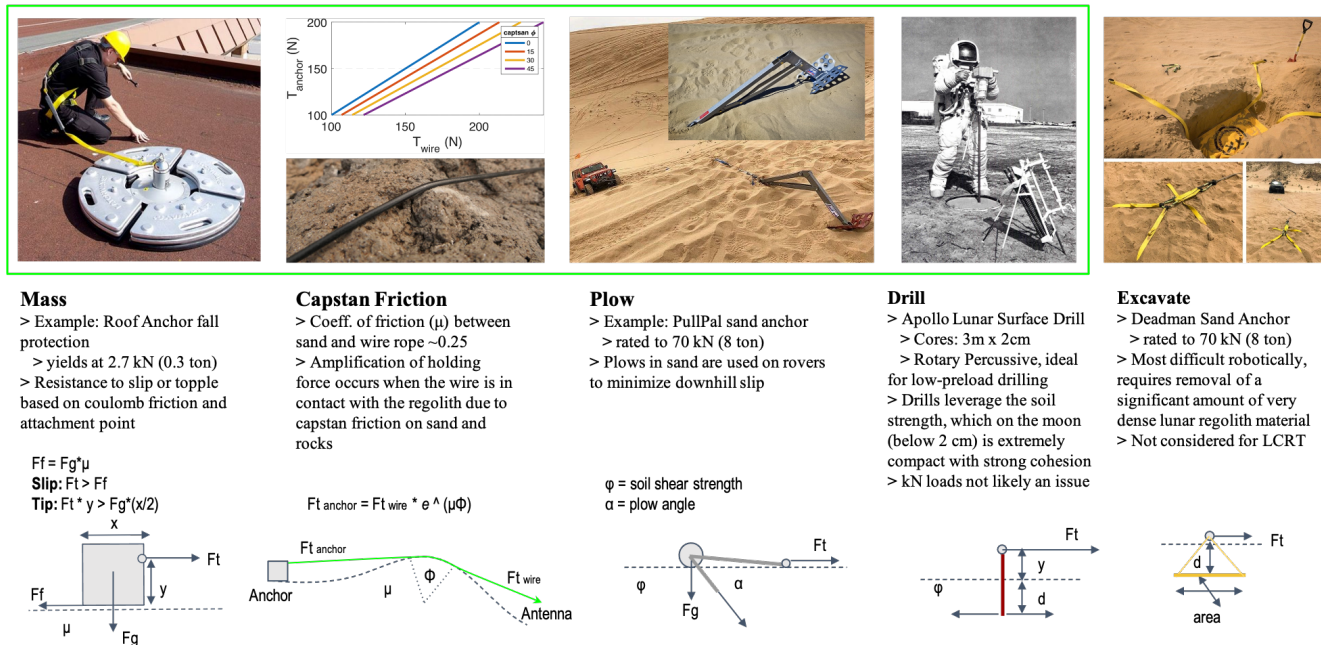> Not considered for LCRT

Figure 45: Details of the different anchoring options. For Plow, Drill, and Excavate methods, anchoring performance requires a complex estimation assuming granular media.
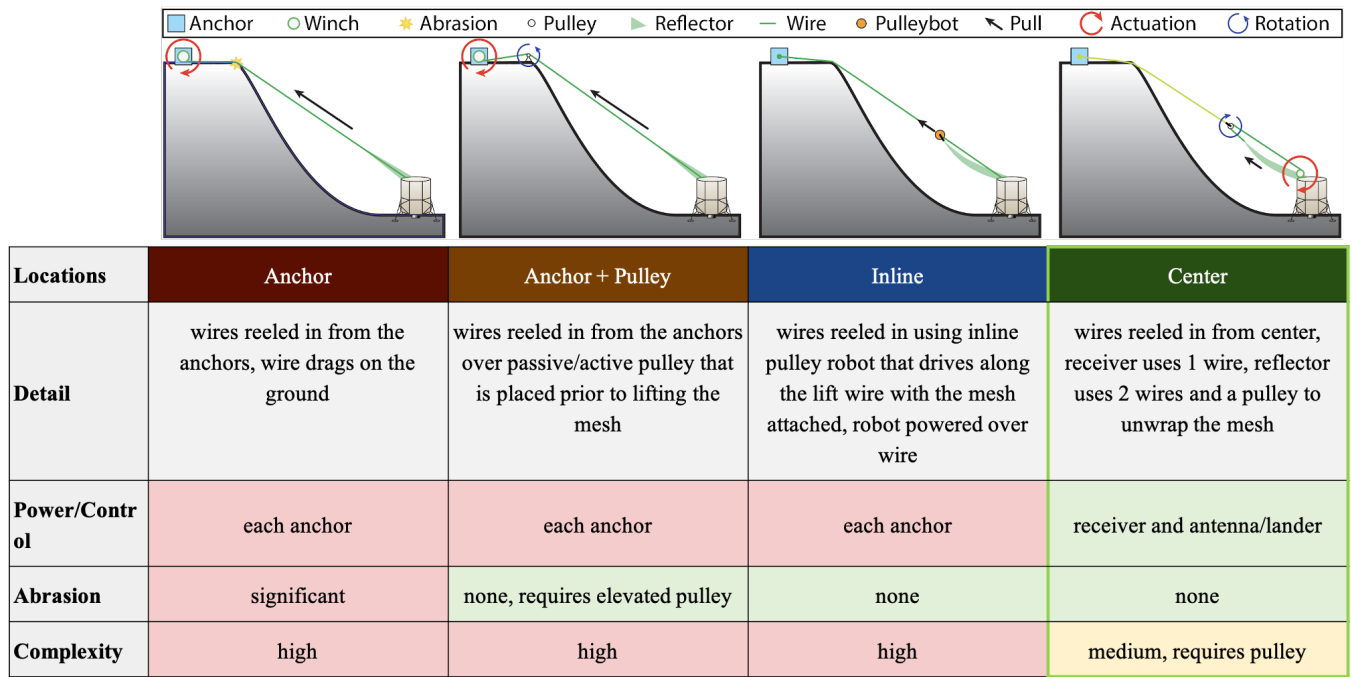
Locations	Anchor	Anchor + Pulley	Inline	Center
Detail	wires reeled in from the anchors, wire drags on the ground	wires reeled in from the anchors over passive/active pulley that is placed prior to lifting the mesh	wires reeled in using inline pulley robot that drives along the lift wire with the mesh attached, robot powered over wire	wires reeled in from center, receiver uses 1 wire, reflector uses 2 wires and a pulley to unwrap the mesh
Power/Control	each anchor	each anchor	each anchor	receiver and antenna/lander
Abrasion	significant	none, requires elevated pulley	none	none
Complexity	high	high	high	medium, requires pulley

Figure 46: Comparison of different lifting locations
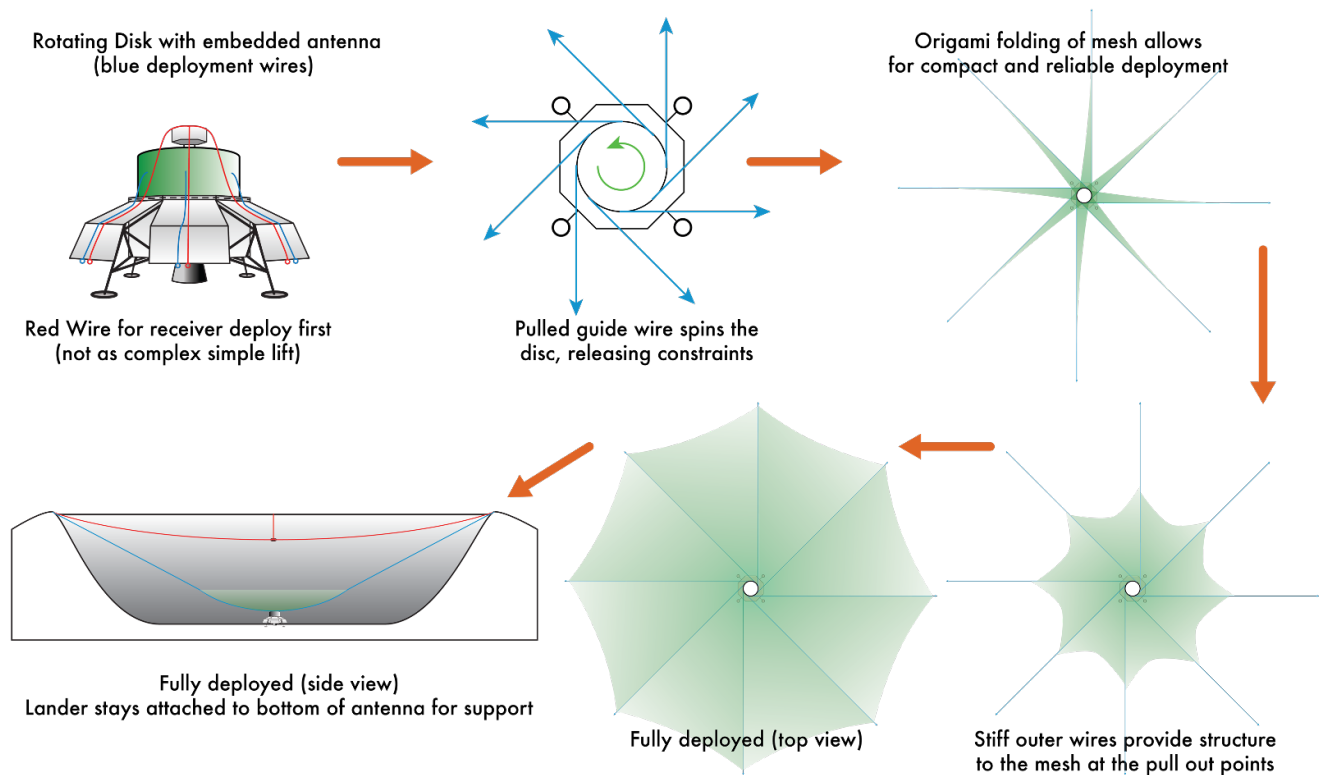

Figure 47: Origami-based deployment process of LCRT's reflector

Finite Element Analysis (FEA) of Reflector Deployment

Deployment of the mesh-origami structure shown in Fig. 47 is demonstrated at a small scale (76 m) and in micro-gravity using Abaqus FEA. The FEA process described is Fig. 24 is used to import the model summarized Fig. 48.
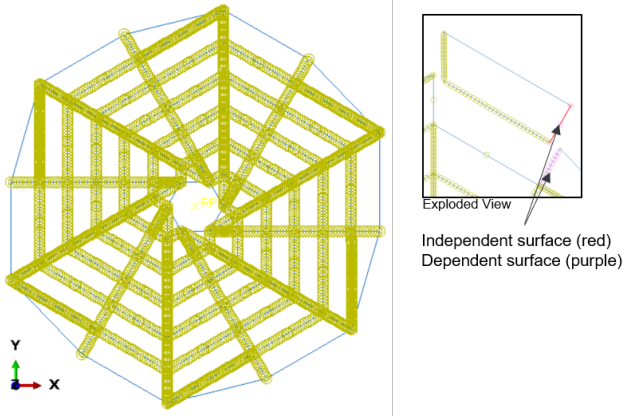

Figure 48: FEA model of the origami structure (simpler pattern for clarity). Each thick yellow line corresponds to surface tied constraints. The exploded view shows details on the constraint where the relative displacement of the dependent surface is controlled by the independent surface while relative rotations are allowed.

Each face of the pattern is a 1 mm diameter aluminum frame made of beam elements. In this preliminary design frames are used to be consistent with the sheet faces of the original origami structure. The pattern has 12 major and 15 minor fold lines. The stowed height and diameter are both 10 m. The fine mesh reflector isn't modeled as assumed compliant. The stowed and deployed FEA models are shown in Fig. 49 and Fig. 50 respectively.
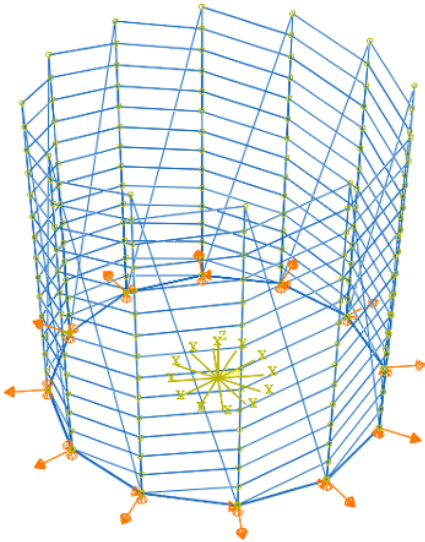

Figure 49: FEA model - stowed structure

This structure has two stable equilibrium, the packaged and deployed configurations. In between deployment is triggered by radially pulling on 12 outer edge points, the inner edge
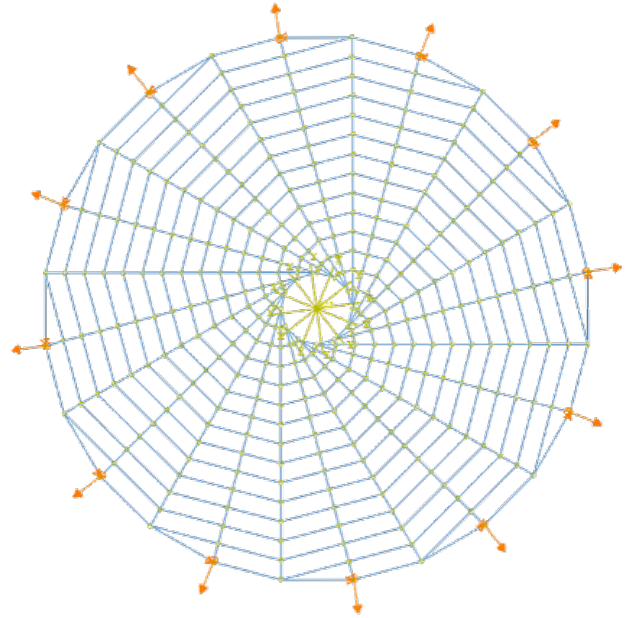

Figure 50: FEA model - deployed structure

being free. The first step of the simulation is static and displacement controlled (series of equilibrium) and the reaction force is shown Fig. 51 for different cable radii r (deployment percentage is computed as the variation of diameter relative to the maximum diameter variation). In particular this shows that radial load scales more or less like r^4, as shown in Fig. 52. Intermediate states of deployment are shown Fig. 53 for 1 mm diameter cables. Around 90.3 % deployment the pulling force becomes negative. At this point the structure fully deploys without external work.
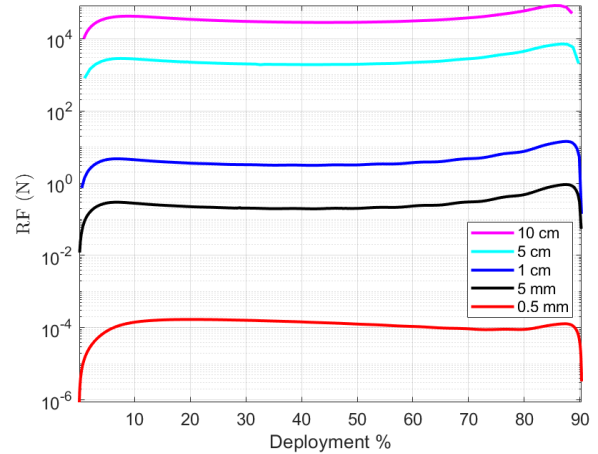
Figure 51: Simulated pulling force profile at one edge during the first stage deployment for various cable radii.

As the cables between the edge of the origami structure and the rim of the carter do not sustain compression, we model this second stage deployment without radial boundary conditions on the outer edge and using a dynamic implicit step. The structure deploys in about 240 seconds and intermediate stages of deployment are shown Fig. 54. Note
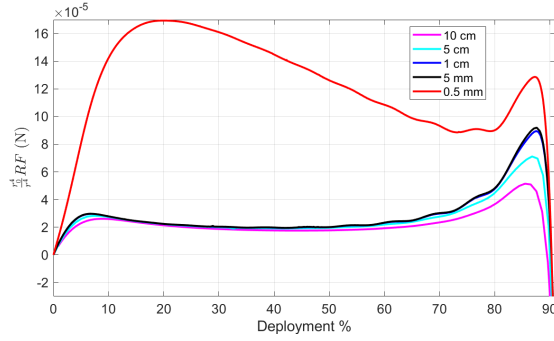
19

Figure 52: Same plot at Fig. 51, but scaled by r^4, with r_0=0.5 mm.
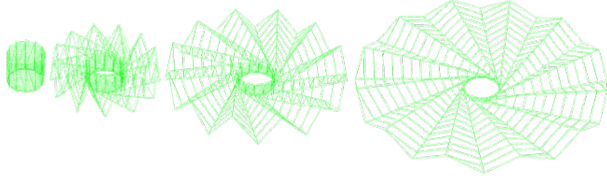

Figure 53: Simulated structure at intermediate stages of deployment during the first quasi-static step at 0%, 30%, 60%, and 90% of deployment from left to right.

that only numerical damping is included in this simulation and residual kinetic energy is still present at 200 sec. Quasi-static deployment are generally preferred and could possibly be achieved by adding a resisting torsional spring at the hub to add stiffness in the structure.
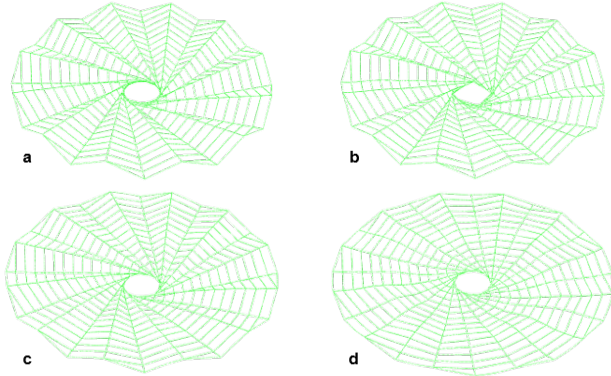

Figure 54: Simulated structure at intermediate stages of the second step dynamic deployment, a: 0 sec, b: 70 sec, c: 140 sec, and d: 200.

Next, we analysed the impact of the major fold (N) and minor fold (n) for constant deployed size is shown in Fig. 55. No exact scaling was found as the results have same order of magnitude. But the snap-through happens slightly later for higher N.

Some significant challenges remain to scale up to 1 km and add gravity. In particular when it comes to the computation time and structural instability as it becomes more slender (thin cables at large scale). Two improvements of the process can be considered and include using truss elements and CYCLSYM multi-point constraints to take advantage of the cyclic symmetry of the pattern.

	Config 1 (red)	Config 2 (blue)
N	12	24
n	15	30
Stowed height	9.7m	5m
Stowed diameter	10.1m	10m
Deployed dia.	75.9m	78m

Table 3: Two configurations for parametric analysis of major folds (N) and minor folds (n)
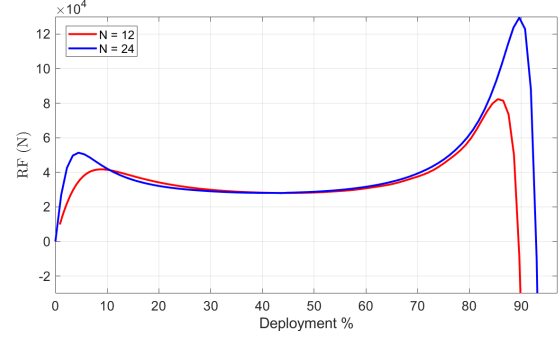

Figure 55: Parametric analysis of the major fold (N) and minor fold (n) for two configurations described in Table 3. The mesh is made of Aluminium and wire radius is 10 cm.

In addition to Abaqus, MERLIN2 [50] – which is a reduced-order structural modeling code for origami-inspired structures – was used to study the deployment of a mesh that has been stowed using a wrapping fold pattern. As with the Abaqus studies, the fold pattern for the mesh follows established approaches [51], [52], and consists of nearly tangential mountain and valley folds that allow the mesh to be wrapped around a central polygonal prism hub.

MERLIN2 uses a bar-and-hinge model for origami structures; the fold lines are modeled as 1D elastic bars, and elastic rotational hinges are placed along the fold and bend lines, modeling the bending stiffness of creases and panels. For this study, small increments of radially outwards displacements were imposed at each valley vertex on the perimeter of the stowed structure. MERLIN2 uses a nonlinear iterative Newton-Rhapson procedure to solve for equilibrium conditions at each increment of displacement – generating a series of equilibria from the stowed condition to the deployed configuration.

Fig. 56 shows the deployment of a 1012 m-diameter structure simulated using this approach. The paraboloid structure has 18-fold rotational symmetry and a focal length of 1000 m. In this simulation, each bar that represents a fold line was assigned a Young's modulus of 70 GPa, and a cross-sectional area of 100 mm2. The structure follows a deterministic deployment path. Fig. 57 shows the magnitude of the radially-outwards force at each of the 18 valley perimeter vertices required to unfold the structure, as a function of deployed radius.

For this initial study, gravity forces were not considered. (In a displacement-controlled MERLIN2 simulation such as this, force-based loading cannot be applied to structure.) As such, the predictions of force required to unfold such a structure are not applicable to a lunar gravity environment. Future iterations of these models will incorporate gravity loading.
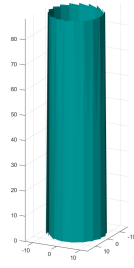
(a) Shows the mesh stowed in a cylindrical volume, 21 m in diameter and 88 m tall.
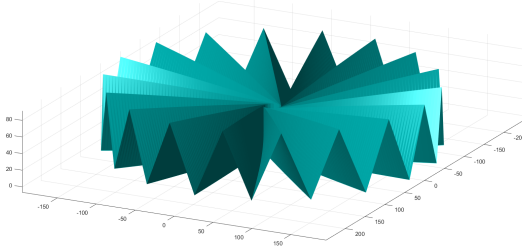
(b) Shows the structure in mid deployment
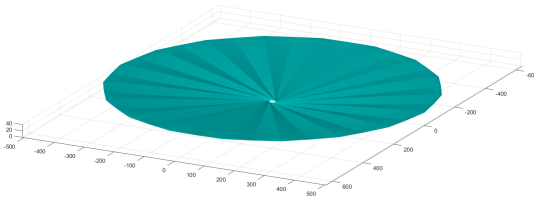
(c) Shows the structure has fully deployed

Figure 56: The deployment of a 1012 m-diameter parabolic mesh structure, simulated using reduced-order modeling in MERLIN2 [50]. The axes have units of meters. Note that future iterations of the fold pattern could be made to stow in much smaller heights by using the approaches laid out by previous work [51].

This reduced-order modeling was conducted to show initial feasibility of stowing and deploying – in a deterministic and non-chaotic manner – a kilometer-scale structure.

6. CONCLUSION

We have described the LCRT concept and the key technical challenges that we need to overcome to make this a reality. We have presented in detail the science objectives and key technology challenges that are at the core of the this mission concept. In this paper, we have not discussed other robotic challenges like communication from Moon's far-side, surviving super-fine lunar dust, power and thermal issues; which are being investigated by other missions across NASA.

If successful, LCRT would provide ground-breaking scientific insights into the evolution of the Universe by observing
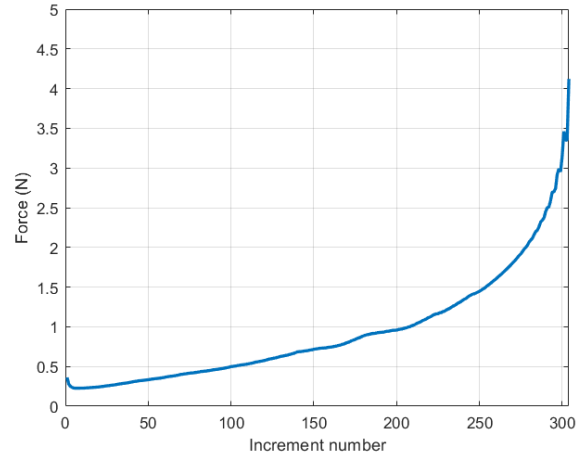

Figure 57: The force required at each of the 18 perimeter valley vertices to unfold the structure shown in Fig. 56, as a function of deployed radius. This calculation does not account for gravity loading that would be present in a lunar environment.

the Universe in the poorly-explored 10–100 m wavelength band. LCRT would be the largest filled-aperture telescope in the Solar System. We envisage that LCRT will open a new window for humanity's exploration of the Universe.

REFERENCES

[1] R. Giovanelli, M. P. Haynes, B. R. Kent, P. Perillat, A. Saintonge, N. Brosch, B. Catinella, G. L. Hoffman, S. Stierwalt, K. Spekkens *et al.*, "The Arecibo legacy fast ALFA survey. I. science goals, survey design, and strategy," *The astronomical journal*, vol. 130, no. 6, p. 2598, 2005.

[2] R. Nan, "Five hundred meter aperture spherical radio telescope (FAST)," *Science in China series G*, vol. 49, no. 2, pp. 129–148, 2006.

[3] J. O. Burns, N. Duric, G. J. Taylor, and S. W. Johnson, "Observatories on the moon," *Scientific American*, vol. 262, no. 3, pp. 42–49, 1990.

[4] S. W. Johnson, "Engineering for a 21st century lunar observatory," *Journal of Aerospace Engineering*, vol. 1, no. 1, pp. 35–51, 1988.

[5] J. Burns, G. Hallinan, J. Lux, A. Romero-Wolf, T.-C. Chang, J. Kocz, J. Bowman, R. MacDowall, J. Kasper, R. Bradley *et al.*, "Farside: A low radio frequency interferometric array on the lunar farside," *arXiv preprint arXiv:1907.05407*, 2019.

[6] P.-Y. Bely, R. J. Laurance, S. Volonte, R. R. Ambrosini, A. van Ardenne, C. H. Barrow, J.-L. Bougeret, J.-M. Marcaide, and G. Woan, "Very low frequency array on

the lunar far side," European Space Agency, Tech. Rep., 1997.

[7] T. J. W. Lazio, R. MacDowall, J. O. Burns, D. Jones, K. Weiler, L. Demaio, A. Cohen, N. P. Dalal, E. Polisensky, K. Stewart *et al.*, "The radio observatory on the lunar surface for solar studies," *Advances in Space Research*, vol. 48, no. 12, pp. 1942–1957, 2011.

[8] T. J. W. Lazio, J. Burns, D. Jones, J. Kasper, S. Neff, R. MacDowall, K. Weiler *et al.*, "The dark ages lunar interferometer (DALI) and the radio observatory for lunar sortie science (ROLSS)," in *Bulletin of the American Astronomical Society*, vol. 41, 2009, p. 344.

[9] J. O. Burns, "The lunar observer radio astronomy experiment (LORAE)," in *Low frequency astrophysics from space*. Springer, 1990, pp. 19–28.

[10] J. O. Burns, J. Lazio, J. Bowman, R. Bradley, C. Carilli, S. Furlanetto, G. Harker, A. Loeb, and J. Pritchard, "The dark ages radio explorer (DARE)," in *Bulletin of the American Astronomical Society*, vol. 43, 2011.

[11] D. Jones, K. Weiler, R. Allen, M. Desch, W. Erickson, M. Kaiser, N. Kassim, T. Kuiper, M. Mahoney, K. Marsh *et al.*, "The astronomical low-frequency array (ALFA)," in *IAU Colloq. 164: Radio Emission from Galactic and Extragalactic Compact Sources*, vol. 144, 1998, p. 393.

[12] J. E. Bergman, R. J. Blott, A. B. Forbes, D. A. Humphreys, D. W. Robinson, and C. Stavrinidis, "FIRST Explorer–an innovative low-cost passive formation-flying system," *arXiv preprint arXiv:0911.0991*, 2009.

[13] R. T. Rajan, A.-J. Boonstra, M. Bentum, M. Klein-Wolt, F. Belien, M. Arts, N. Saks, and A.-J. van der Veen, "Space-based aperture array for ultra-long wavelength radio astronomy," *Experimental Astronomy*, vol. 41, no. 1-2, pp. 271–306, 2016.

[14] R. D. Blandford *et al.*, *New Worlds, New Horizons in Astronomy and Astrophysics*. The National Academies Press, Washington, DC, 2010.

[15] C. Kouveliotou, E. Agol, N. Batalha, J. Bean, M. Bentz, N. Cornish, A. Dressler, E. Figueroa-Feliciano, S. Gaudi, O. Guyon *et al.*, "Enduring quests-daring visions (NASA astrophysics in the next three decades)," *arXiv preprint arXiv:1401.3741*, 2014.

[16] A. Datta, R. Bradley, J. O. Burns, G. Harker, A. Komjathy, and T. J. W. Lazio, "The effects of the ionosphere on ground-based detection of the global 21 cm signal from the cosmic dawn and the dark ages," *The Astrophysical Journal*, vol. 831, no. 1, p. 6, 2016.

[17] E. Shen, D. Anstey, E. de Lera Acedo, A. Fialkov, and W. Handley, "Quantifying ionospheric effects on global 21-cm observations," *arXiv preprint arXiv:2011.10517*, 2020.

[18] B. E. Robertson, R. S. Ellis, J. S. Dunlop, R. J. McLure, and D. P. Stark, "Early star-forming galaxies and the reionization of the universe," *Nature*, vol. 468, no. 7320, pp. 49–55, 2010.

[19] S. R. Furlanetto, S. P. Oh, and F. H. Briggs, "Cosmology at low frequencies: The 21cm transition and the high-redshift universe," *Physics Reports*, vol. 433, no. 4, pp. 181–301, 2006.

[20] J. R. Pritchard and A. Loeb, "21cm cosmology in the 21st century," *Reports on Progress in Physics*, vol. 75, no. 8, p. 086901, 2012.

[21] R. Srianand, P. Petitjean, and C. Ledoux, "The cosmic microwave background radiation temperature at a redshift of 2.34," *Nature*, vol. 408, no. 6815, pp. 931–935, 2000.

[22] J. C. Pober, Z. S. Ali, A. R. Parsons, M. McQuinn, J. E. Aguirre, G. Bernardi, R. F. Bradley, C. L. Carilli, C. Cheng, D. R. DeBoer *et al.*, "64 constraints on reionization. II. the temperature of the z=8.4 intergalactic medium," *The Astrophysical Journal*, vol. 809, no. 1, p. 62, 2015.

[23] Z. S. Ali, A. R. Parsons, H. Zheng, J. C. Pober, A. Liu, J. E. Aguirre, R. F. Bradley, G. Bernardi, C. L. Carilli, C. Cheng *et al.*, "64 constraints on reionization: The 21cm power spectrum at z=8.4," *The Astrophysical Journal*, vol. 809, no. 1, p. 61, 2015.

[24] R. A. Monsalve, A. E. Rogers, J. D. Bowman, and T. J. Mozdzen, "Results from edges high-band: I. constraints on phenomenological models for the global 21cm signal," *The Astrophysical Journal*, vol. 847, no. 64, p. 12pp, 2017.

[25] S. Furlanetto, J. D. Bowman, J. Mirocha, J. C. Pober, J. Burns, C. L. Carilli, J. Munoz, J. Aguirre, Y. Ali-Haimoud, M. Alvarez, A. Beardsley, G. Becker, P. Breysse, V. Bromm, P. Bull, T.-C. Chang, X. Chen, H. Chiang, J. Cohn, F. Davies, D. DeBoer, J. Dillon, O. Doré, C. Dvorkin, A. Fialkov, B. Hazelton, D. Jacobs, K. Karkare, S. Kohn, L. Koopmans, E. Kovetz, P. L. Plante, A. Lidz, A. Liu, Y.-Z. Ma, Y. Mao, K. Masui, A. Mesinger, S. Murray, A. Parsons, B. Saliwanchik, J. Sievers, N. Thyagarajan, H. Trac, E. Visbal, and M. Zaldarriaga, "Astro 2020 science white paper: Fundamental cosmology in the dark ages with 21-cm line fluctuations," *arXiv preprint arXiv:1903.06212*, 2019.

[26] J. D. Bowman, A. E. Rogers, R. A. Monsalve, T. J. Mozdzen, and N. Mahesh, "An absorption profile centred at 78 megahertz in the sky-averaged spectrum," *Nature*, vol. 555, no. 7694, pp. 67–70, 2018.

[27] J. O. Burns, S. Bale, N. Bassett, J. Bowman, R. Bradley, A. Fialkov, S. Furlanetto, M. Hecht, M. Klein-Wolt, C. Lonsdale *et al.*, "Dark cosmology: Investigating dark matter & exotic physics in the dark ages using the redshifted 21-cm global spectrum," *arXiv preprint arXiv:1902.06147*, 2019.

[28] N. Bassett, D. Rapetti, J. O. Burns, K. Tauscher, and R. MacDowall, "Characterizing the radio quiet region behind the lunar farside for low radio frequency experiments," *arXiv preprint arXiv:2003.03468*, 2020.

[29] B. Burke and K. Franklin, "Observations of a variable radio source associated with the planet Jupiter," *Journal of Geophysical Research*, vol. 60, no. 2, pp. 213–217, 1955.

[30] K. Franklin and B. Burke, "Radio observations of Jupiter." *The Astronomical Journal*, vol. 61, p. 177, 1956.

[31] N. Gopalswamy, "Recent advances in the long-wavelength radio physics of the sun," *Planetary and Space Science*, vol. 52, no. 15, pp. 1399–1413, 2004.

[32] F. Alibay, T. J. W Lazio, J. C. Kasper, and T. Neilsen, "Sun radio interferometer space experiment (sunrise) proposal: Status update," Aug. 2017.

[33] M. Kaiser, M. Desch, J.-L. Bougeret, R. Manning, and C. Meetre, "WIND/WAVES observations of man-

made radio transmissions," *Geophysical research letters*, vol. 23, no. 10, pp. 1287–1290, 1996.

[34] J.-L. Bougeret, K. Goetz, M. Kaiser, S. Bale, P. Kellogg, M. Maksimovic, N. Monge, S. Monson, P. Astier, S. Davy *et al.*, "S/WAVES: the radio and plasma wave investigation on the STEREO mission," *Space Science Reviews*, vol. 136, no. 1-4, pp. 487–528, 2008.

[35] D. Rapetti, K. Tauscher, J. Mirocha, and J. O. Burns, "Global 21 cm signal extraction from foreground and instrumental effects. ii. efficient and self-consistent technique for constraining nonlinear signal models," *The Astrophysical Journal*, vol. 897, no. 2, p. 174, 2020.

[36] K. Tauscher, D. Rapetti, J. O. Burns, and E. Switzer, "Global 21 cm signal extraction from foreground and instrumental effects. i. pattern recognition framework for separation using training sets," *The Astrophysical Journal*, vol. 853, no. 2, p. 187, 2018.

[37] M. S. Rao, R. Subrahmanyan, N. U. Shankar, and J. Chluba, "Modeling the radio foreground for detection of cmb spectral distortions from the cosmic dawn and the epoch of reionization," *The Astrophysical Journal*, vol. 840, no. 1, p. 33, 2017.

[38] A. Liu, J. R. Pritchard, M. Tegmark, and A. Loeb, "Global 21cm signal experiments: A designer's guide," *Physical Review D*, vol. 87, no. 4, p. 043002, 2013.

[39] J. Lazio, *Radio Observations as an Exoplanet Discovery Method*. Berlin: Springer, 2017.

[40] T. J. W. Lazio, E. Shkolnik, G. Hallinan, P. H. S. Team *et al.*, "Planetary magnetic fields: Planetary interiors and habitability," *Planetary Magnetic Fields: Planetary Interiors and Habitability, Final Report funded by the Keck Institute for Space Studies, 2016, 147pp.*, 2016.

[41] S. J. Robbins, "A new global database of lunar impact craters¿ 1–2 km: 1. crater locations and sizes, comparisons with published databases, and global analysis," *Journal of Geophysical Research: Planets*, vol. 124, no. 4, pp. 871–892, 2019.

[42] R. Osserman, "Mathematics of the gateway arch," *Notices of the AMS*, vol. 57, no. 2, pp. 220–229, 2010.

[43] V. Vanzani, F. Marzari, and E. Dotto, "Micrometeoroid impacts on the lunar surface," *LPI*, p. 1481, 1997.

[44] R. P. Hoyt and R. L. Forward, "Failure resistant multiline tether," Jan. 16 2001, uS Patent 6,173,922.

[45] J.-P. Williams, D. Paige, B. Greenhagen, and E. Sefton-Nash, "The global surface temperatures of the moon as measured by the diviner lunar radiometer experiment," *Icarus*, vol. 283, pp. 300–325, 2017.

[46] J. Kinast, E. Hilpert, N. Lange, A. Gebhardt, R.-R. Rohloff, S. Risse, R. Eberhardt, and A. Tünnermann, "Minimizing the bimetallic bending for cryogenic metal optics based on electroless nickel," in *Advances in Optical and Mechanical Technologies for Telescopes and Instrumentation*, vol. 9151. International Society for Optics and Photonics, 2014, p. 915136.

[47] P. McGarey, S. Bandyopadhyay, R. Rafizadeh, A. Goel, M. Arya, I. Nesnas, J. Lazio, P. Goldsmith, A. Stoica, M. Quadrelli, and G. Hallinan, "A concept for the deployment of a large lunar crater radio telescope on the moon using teams of tethered robots," in *International Symposium on Artificial Intelligence, Robotics and Automation in Space (i-SAIRAS)*, 2020.

[48] R. Weber, J. Alexander, and R. Stone, "The Radio Astronomy Explorer satellite, a low-frequency observatory," *Radio Science*, vol. 6, no. 12, pp. 1085–1097, 1971.

[49] M. Arya, D. Webb, J. Steeves, P. D. Lisman, P. A. Willems, S. C. Bradford, E. Kelso, K. Neff, N. Beidleman, J. D. Stienmier *et al.*, "Demonstration of deployment accuracy of the starshade inner disk subsystem," in *AIAA Scitech 2020 Forum*, 2020, p. 1670.

[50] K. Liu and G. Paulino, "Highly efficient nonlinear structural analysis of origami assemblages using the MERLIN2 software," *Origami*, vol. 7, pp. 1167–1182, 2018.

[51] S. A. Zirbel, R. J. Lang, M. W. Thomson, D. A. Sigel, P. E. Walkemeyer, B. P. Trease, S. P. Magleby, and L. L. Howell, "Accommodating thickness in origami-based deployable arrays," *Journal of Mechanical Design*, vol. 135, no. 11, 2013.

[52] M. Arya, D. Webb, S. C. Bradford, L. Adams, V. Cormarkovic, G. Wang, M. Mobrem, K. Neff, N. Beidleman, J. D. Stienmier *et al.*, "Origami-inspired optical shield for a starshade inner disk testbed: design, fabrication, and analysis," in *AIAA Scitech 2021 Forum, 8th Spacecraft Structures Conference*, 2021.

Saptarshi Bandyopadhyay *is a Robotics Technologist at the NASA Jet Propulsion Laboratory, California Institute of Technology, where he develops novel algorithms for future multi-agent and swarm missions. He was recently named a NIAC fellow for his work on the Lunar Crater Radio Telescope on the far-side of the Moon. He received his Ph.D. in Aerospace Engineering in 2016 from the University of Illinois at Urbana-Champaign, USA, where he specialized in probabilistic swarm guidance and distributed estimation. He earned his Bachelors and Masters degree in Aerospace Engineering in 2010 from the Indian Institute of Technology Bombay, India, where as an undergraduate, he co-founded and led the institute's student satellite project Pratham, which was launched into low Earth orbit in September 2016. His engineering expertise stems from a long-standing interest in the science underlying space missions, since winning the gold medal for India at the 9th International Astronomy Olympiad held in Ukraine in 2004. Saptarshi's current research interests include robotics, multi-agent systems and swarms, dynamics and controls, estimation theory, probability theory, and systems engineering. He has published more than 40 papers in journals and refereed conferences.*

Patrick McGarey *is a Robotics Technologist at JPL in the Robotic Mobility Group. Patrick received his PhD in Aerospace Engineering from the University of Toronto, where he was a visiting Fulbright Scholar. His research is focused on the development of systems and autonomy functions for the exploration of extreme environments throughout the solar system. Currently, Patrick is working on the Axel/DuAxel rover to enable advanced mobility for the exploration of RSL features on Mars and lava tubes on the Moon.*

Ashish Goel is a Research Technologist at the Jet Propulsion Laboratory in the Robotic Surface Mobility group. Ashish received his Masters and PhD in Aeronautics and Astronautics from Stanford University where he worked with Prof. Sigrid Close, developing sensors and techniques for the detection and characterization of meteoroid and orbital debris impacts in space. He received his bachelor's degree in Engineering Physics from Indian Institute of Technology Bombay. Prior to joining JPL, Ashish also worked as a postdoctoral researcher with Prof. Sergio Pellegrino in the Graduate Aerospace Laboratories at Caltech. He developed optimized trajectories for a planar formation of space solar power satellites. He also served as a systems engineer and worked on the design of flight electronics for the Autonomous Assembly of a Reconfigurable Space Telescope (AAReST) project.

Manan Arya is a Technologist in the Advanced Deployable Structures group at the Jet Propulsion Laboratory. He received his PhD in Aerospace Engineering from the California Institute of Technology, where he developed novel breakthrough schemes for the packaging and deployment of large lightweight spacecraft structures under the guidance of Prof. Sergio Pellegrino. He holds a Master's degree in Aerospace Engineering from Caltech and a Bachelor's degree in Applied Science in Engineering Science from the University of Toronto. His research interests include origami-inspired structures for spacecraft, ultralightweight composite materials, and ground testing of large unfoldable structures.

Ramin Rafizadeh is a Systems Engineer at the Jet Propulsion Laboratory in the Systems Integrations and Test group working on Assembly, Test, and Launch Operations (ATLO) for the Europa Clipper mission. He graduated with Honors in Aerospace Engineering from the University of Maryland College Park, Clark School of Engineering. His primary research focus was centered around autonomous space robotics where he had key roles in multiple labs such as the Space Systems Laboratory (SSL) and the Collective Dynamics and Control Lab (CDCL). Prior to joining JPL, he was also a member of the Engineering and Robotics Laboratory at the National Institute of Standards and Technology (NIST) where he researched cybersecurity implementation for Industrial Control Systems and produced guidelines implementing specific measures in order to create a safer environment. He has completed two internships with NASA's Jet Propulsion Laboratory. During his first internship, he supported the Mars Science Laboratory's Curiosity Rover sampling system team. The following year he was invited back to serve as a Co-Investigator on this study and supported CubeSat R&D in the Mobility and Robotic Systems Multi-Agent Autonomy group which demonstrated novel technologies never flown before.

Joseph Lazio is Chief Scientist of the Interplanetary Network Directorate at the Jet Propulsion Laboratory, California Institute of Technology. The Interplanetary Network Directorate manages the Deep Space Network for NASA's Space Communications and Navigation (SCaN) Division. He received his Ph.D. from Cornell University, was a U.S. National Research Council Research Associate at the U.S. Naval Research Laboratory, and was a Radio Astronomer on the staff of the U.S. NRL, before joining JPL. He is the Project Scientist for the Sun Radio Interferometer Space Experiment and was the Deputy Principal Investigator for the proposed Dark Ages Radio Explorer (DARE). He has served as Project Scientist for the Square Kilometre Array (SKA); the Deputy Director of the Lunar University Network for Astrophysics Research (LUNAR); and as Project Scientist for the U.S. Virtual Astronomical Observatory. He also observes routinely with the world's premier ground based radio telescopes, including the Expanded Very Large Array, the Very Long Baseline Array, the Green Bank Telescope, the Giant Metrewave Radio Telescope, and the Australia Telescope Compact Array.

Melanie Delapierre is a Postdoctoral Scholar in the Dynamics and Structures group at the Jet Propulsion Laboratory. She received her PhD in Space Engineering from the California Institute of Technology, where she studied the dynamics and stability of spinning membranes as novel space structures. She holds a Master's degree in Space Engineering from Caltech and a Bachelor's degree in Mechanical Engineering from Ecole Polytechnique in France. Her research interests include deployment of lightweight structures and topology optimization.

Paul Goldsmith is Senior Research Scientist and Group Supervisor at JPL. His recent work has focused on determining time scales of processes associated with the formation of molecular clouds and young stars. This has included use of atomic hydrogen in molecular clouds as a tracer of their evolution and history. Goldsmith has also worked on determining the conditions for formation of massive stars by using molecular line and dust continuum emission. He has also been using specific tracers of chemistry in the interstellar medium to assess the impact of star formation on surrounding molecular cloud material via heating of dust, shock waves, and other processes. Goldsmith is the Project Scientist for GUSTO, a NASA Balloon mission that will map the Milky Way in three critical fine structure lines following its launch in 2021.

Nacer Chahat received the Master's degree in electrical engineering from the Ecole Supérieur d'ingénieurs de Rennes (ESIR), Rennes, France, in 2009; the Master's degree in telecommunication and the Ph.D. degree in signal processing and telecommunications from the Institute of Electronics and Telecommunications of Rennes (IETR), University of Rennes 1, Rennes, France, in 2009 and 2012, respectively. He is a Senior Antenna/Microwave Engineer with the National Aeronautics and Space Administration (NASA) Jet Propulsion Laboratory (JPL), California Institute of Technology, Pasadena, CA. Since 2013, he has been a Microwave/Antenna Engineer with NASA's Jet Propulsion Laboratory and he has been Technical Section Staff. He is currently the Payload System Engineer lead on the SWOT mission. He has authored and coauthored more than 100 technical journal articles and conference papers, has written four book chapters, and also holds several patents. His research interests include deployable antennas for CubeSat and small satellites, spacecraft antennas for telecommunications, RADAR, imaging systems, metasurface antennas and metasurface beam steering antennas.

Adrian Stoica has thirty years of R&D experience in autonomous systems, developing novel adaptive, learning and evolvable hardware techniques and embedding them into electronics and intelligent information systems, for applications ranging from measurement equipment to space avionics to robotics. He has done pioneering work in humanoid robot learning by imitation, hardware security including anti-tamper, brain-computer interfaces including multi-brain fusion for joint decision making, shadow biometrics, shape-changing robots, human-oriented robotics. He is a member of the board of Governors of IEEE Systems, Man, and Cybernetics Society (since 2015). He founded 3 conferences: NASA/ESA Conference on Adaptive Hardware and Systems (AHS, since 1999), Emerging Security Technologies (since 2006) and the AT-EQUAL series (Advanced Technologies for Enhanced Quality of Life) which included the HUMASCEND conference (Human-Machine Systems, Cyborgs and Enhancing Devices 2011-2014). He is currently the Group Supervisor of the Robotic Systems Estimation, Decision, and Control Group at JPL, Caltech and a NIAC Fellow in 2013 and 2015.

Marco Quadrelli has been at the Jet Propulsion Laboratory, California Institute of Technology since 1997, where he has worked as Research Technologist in the Mobility and Robotic Systems Section and in the Guidance and Control Section. He has been a visiting scientist at the Harvard-Smithsonian Center for Astrophysics, did post-doctoral work in computational micro-mechanics at the Institute of Paper Science and Technology in Atlanta, and has been a Lecturer in Aerospace Engineering both at JPL and at the Caltech Graduate Aeronautical Laboratories. He has been involved in spacecraft stability, dynamics and control of tethered space systems, formation flying, distributed spacecraft and robots, inflatable apertures, hypersonic entry and aero-maneuvering, precision landing with controlled decelerators, adaptive structures for planetary sampling, and guidance, navigation and control of spacecraft swarms.

Issa Nesnas is a principal technologist and the supervisor of the Robotic Mobility group at the Jet Propulsion Laboratory with over two decades of research in space robotics and industrial automation. He leads research in autonomy and mobility with a focus on extreme terrain access and microgravity mobility. He contributed to the development of autonomous rover navigation and visual target tracking and participated in the development of the Curiosity and Mars 2020 rovers. Dr. Nesnas served on NASA's Capability Leadership Team for Autonomy and was the co-chair for NASA's Technology Roadmaps for Robotics and Autonomous Systems. He holds several patents and has over fifty publications in this field. He holds a B.E. degree in Electrical Engineering from Manhattan College and a M.S. and Ph.D. in Mechanical Engineering with a specialization in robotics from the University of Notre Dame.

Kenneth Jenks has over three decades of experience at NASA. He conducts research in cable-crawler robotics. He wrote software for the Space Shuttle Remote Manipulator System (RMS), including the RMS Situation Awareness Display (RSAD) and the Bird's Eye View (BEV) prototype, the first Virtual Reality application flown in space. He contributed to NASA artificial intelligence software for Mission Control and to the development of Robonaut R1A, a humanoid robot, part of a development project conducted by the Dexterous Robotics Laboratory at NASA's Johnson Space Center.

Gregg Hallinan is Professor of Astronomy at Caltech, and Director of the Owens Valley Radio Observatory (OVRO). His primary interests are the magnetic fields of exoplanets, brown dwarfs and stars and all sources of transient radio emission.